



## Progressive damage and rupture in polymers



Brandon Talamini, Yunwei Mao, Lallit Anand\*

Department of Mechanical Engineering, Massachusetts Institute of Technology, Cambridge, MA, 02139, USA

---

### ARTICLE INFO

*Article history:*

Received 10 May 2017

Revised 6 October 2017

Accepted 16 November 2017

Available online 16 November 2017

---

*Keywords:*

Polymers

Damage

Rupture

Phase-field theory

Gradient-damage theory

---

### ABSTRACT

Progressive damage, which eventually leads to failure, is ubiquitous in biological and synthetic polymers. The simplest case to consider is that of elastomeric materials which can undergo large reversible deformations with negligible rate dependence. In this paper we develop a theory for modeling progressive damage and rupture of such materials. We extend the phase-field method, which is widely used to describe the damage and fracture of brittle materials, to elastomeric materials undergoing large deformations. A central feature of our theory is the recognition that the free energy of elastomers is not entirely entropic in nature – there is also an energetic contribution from the deformation of the bonds in the chains. It is the energetic part in the free energy which is the driving force for progressive damage and fracture.

© 2017 Elsevier Ltd. All rights reserved.

---

### 1. Introduction

The development of soft materials for mechanical applications has ushered a recent revolution in materials. Applications often depend on the great extensibility of polymer-based materials, as well as many other useful properties that soft materials can possess, including bio-compatibility, self-healing (Cordier et al., 2008; Holten-Andersen et al., 2010), and novel actuation mechanisms and functions (Tokarev and Minko, 2009). In addition to the traditional engineering uses of elastomeric materials, transformative applications are being developed daily, from surgical adhesives to replace sutures (Duarte et al., 2012), hydrogel scaffolding for tissue engineering (Lee and Mooney, 2001), and artificial cartilage, tendons and ligaments for joint repair therapies (Azuma et al., 2006; Nonoyama et al., 2016). The mechanical demands of these applications places new importance on understanding and modeling of damage and failure of these materials.

Modeling of failure in polymers falls in two broad categories: the first comprises macroscopic “top-down” approaches based on a Griffith-type critical energy release rate criterion. The application of top-down approaches to polymer fracture dates back to Rivlin and Thomas’s work with commercial rubbers (Rivlin and Thomas, 1952). The second category comprises “bottom-up” approaches that investigate the mechanisms of damage at the molecular scale and attempt to build a consistent picture up through larger scales. The second approach has been largely driven by research on biological materials and design of bio-inspired composites (see, e.g., (Baer et al., 1987; Buehler, 2006; Gao, 2006; Jackson et al., 1988; Kamat et al., 2000; Sen and Buehler, 2011; Sun and Bhushan, 2012)). An early attempt at linking these approaches occurs in the landmark paper of Lake and Thomas (1967) in which they proposed a scaling law for the critical energy release rate in terms of microscopic parameters, including the binding energy between monomer units and the chain network mesh size.

One important advantage of the bottom-up approach is the understanding that it provides on the sensitivity of materials to flaws at small length scales. The theory of Griffith governs fracture at the macro-scale, and reveals that the resistance

---

\* Corresponding author.

E-mail address: [anand@mit.edu](mailto:anand@mit.edu) (L. Anand).

of a body to fracture depends sensitively on the size of flaws contained within it (Griffith, 1921). However, the picture is different at very small length scales, since the assumption that the behavior of the crack tip region can be separated from the far-field response, which underpins the Griffith theory, does not hold. Instead, the nonlinear mechanical response of the molecular bonds is felt over the entire body (Buehler et al., 2003), and a large fraction of the material is stressed to levels approaching the ideal strength, rather than just the region near the flaw tip. As a result, the material is much less sensitive to flaws (Chen et al., 2016; Gao et al., 2003; Mao et al., 2017b). The molecular-scale physics is necessary to explain this flaw-insensitive behavior, and bottom-up modeling is necessary to control it and exploit it.

Most of the developments in the bottom-up description of failure in polymers have been conducted through the framework of molecular dynamics (see, e.g., Rottler et al., 2002; Rottler and Robbins, 2003). Unfortunately, the computational demands of molecular dynamics limit the simulated length scales and time durations to scales below those needed for engineering design and optimization. It seems likely that continuum-based approaches will be needed for these purposes for the foreseeable future. Of course, to make a predictive continuum-level model, the underlying molecular physics must be retained to the furthest extent possible. The aim of this paper is to take a step in this direction.

The simplest polymers are elastomeric materials, which consist of a chemically crosslinked network of flexible polymeric chains that can undergo large reversible deformations with negligible rate-dependence. In this paper we develop a continuum theory for modeling progressive damage and rupture of such materials. One of the distinguishing features of elastomers is that their deformation response is dominated by changes in entropy. Accordingly, most classical theories of rubber elasticity consider only changes in entropy due to deformation, and neglect any changes in internal energy (e.g., Kuhn and Grün, 1942; Treloar, 1975; Arruda and Boyce, 1993). On the other hand, as recognized by Lake and Thomas (1967), rupture is an energetic process at the micro-scale, emanating from the scission of molecular bonds in the polymer chains.<sup>1</sup> In order to achieve the microscopic perspective, our theory incorporates a recently proposed hyperelastic model that describes both the entropic elasticity of polymer chains, as well as a description of the mechanics of the molecular bonds in the backbone of the chain (Mao et al., 2017b).

We make use of a phase-field approach to model the loss of stress-bearing capacity of the material due to the softening and rupture of bonds at large stretches. The model describes damage initiation, propagation, and full rupture in polymeric materials. The phase-field acts as a damage variable, with a nonlocal contribution to the free energy that regularizes the theory and sets a length scale for the rupture process.

In its structure, our framework is similar to the top-down phase-field approaches to fracture based on Bourdin et al. (2000) that have become popular over the last 20 years, including several devoted to rupture of elastomeric materials (Miehe and Schäzel, 2014; Raina and Miehe, 2016; Wu et al., 2016). The distinction of our model is in the scale: in the previous works, the phase-field serves as mathematical regularization of the critical energy release rate theory – thus embodying a macroscopic approach – while here we directly consider the physics of bond scission at the local scale. In particular, our work significantly departs from these previous works in the definition of the driving force for damage. The proposed model discriminates between entropic contributions to the free energy due to the configurational entropy of the polymer chains, and the internal energy contributions due to bond deformation. We argue that the evolution of the phase-field should be driven solely by the internal energy, since the microscopic bond scission mechanism it represents is fundamentally an energetic process.

The plan of this paper is as follows. In Section 2 we give a brief summary of the structure of the theory, including the balance laws and the constitutive framework. In Section 3 we specify the constitutive relations of the theory. We proceed step-by-step in the development of the constitutive relations, starting with the deformation response of a single chain with no damage, then proceed to a damage model for softening and scission of a single chain. We discuss how these specific constitutive relations represent a microscopic view of damage in elastomers. Next, we generalize the single chain model to describe the response of bulk material comprised of a network of chains, which bridges the microscopic perspective to the macroscopic one. In Section 5 we study the capability of the model to describe flaw-size sensitivity in single-edge-notched specimens which are sub-millimeter in size, with micron-dimensioned cracks. In Section 6 we show the capability of the theory and numerical simulation capability to model the experimental results of Hocine et al. (2002) on fracture of double-edge-notched specimens of a styrene-butadiene elastomer (SBR) – specimens which are tens of millimeters in size, with millimeter-dimensioned cracks. Finally, we summarize the main conclusions and make some final remarks in Section 7. A full derivation of the balance laws using the principle of virtual power and the development of the thermodynamically consistent constitutive framework are included in Appendix A, and some details of the numerical implementation of the theory are given in Appendix B.

## 2. Summary of the constitutive theory, governing partial differential equations and boundary conditions

We have formulated a phase-field/gradient-damage theory for fracture of a finitely-deforming elastic solid using the pioneering virtual-power approach of Curtin (1996, 2002). This approach leads to “macroforce” and “microforce” bal-

<sup>1</sup> If the cross-linking chemical bonds in an elastomeric network are strong, then fracture is expected to occur by scission of the chains between the crosslinks, as envisioned in the classical model of Lake and Thomas (1967), while if the chemical crosslinks are weak then fracture is expected to occur because of the scission of the cross-linking bonds themselves. In this paper we focus our attention on networks with strong cross-linking bonds which fail by chain-scission.

ances for the forces associated with the rate-like kinematical descriptors in the theory. These macro- and microforce balances, together with a standard free-energy imbalance law under isothermal conditions, when supplemented with a set of thermodynamically-consistent constitutive equations, provide the governing equations for our theory. Our theory, which is developed in detail in [Appendix A](#), is summarized below. It relates the following basic fields:<sup>2</sup>

$\mathbf{x} = \chi(\mathbf{X}, t)$ ,	motion;
$\mathbf{F} = \nabla \chi$ , $J = \det \mathbf{F} > 0$ ,	deformation gradient;
$\bar{\mathbf{F}} = J^{-1/3} \mathbf{F}$ ,	distortional part of $\mathbf{F}$ ;
$\mathbf{C} = \mathbf{F}^\top \mathbf{F}$ ,	right Cauchy-Green tensor;
$\bar{\mathbf{C}} = \bar{\mathbf{F}}^\top \bar{\mathbf{F}} = J^{-2/3} \mathbf{C}$ ,	distortional part of $\mathbf{C}$ ;
$\mathbf{T}_R, \mathbf{T}_R \mathbf{F}^\top = \mathbf{F} \mathbf{T}_R^\top$	Piola stress;
$\mathbf{T}_{RR} = \mathbf{F}^{-1} \mathbf{T}_R$ ,	second Piola stress;
$\psi_R$ ,	free energy density per unit reference volume;
$\varepsilon_R$ ,	internal energy density per unit reference volume;
$\lambda_b > 0$	effective bond stretch (an internal variable);
$d(\mathbf{X}, t) \in [0, 1]$ ,	damage variable, or phase-field;
$\varpi$	scalar microstress conjugate to $d$ ;
$\xi$	vector microstress conjugate to $\nabla d$ .

## 2.1. Constitutive equations

### 1. Free energy

This is given by

$$\psi_R = \hat{\psi}_R(\Lambda), \quad (2.1)$$

with  $\Lambda$  the list

$$\Lambda = \{\mathbf{C}, \lambda_b, d, \nabla d\}. \quad (2.2)$$

### 2. Second Piola stress. Piola stress

The second Piola stress is given by

$$\mathbf{T}_{RR} = 2 \frac{\partial \hat{\psi}_R(\Lambda)}{\partial \mathbf{C}}, \quad (2.3)$$

and the Piola stress by

$$\mathbf{T}_R = \mathbf{F} \mathbf{T}_{RR}. \quad (2.4)$$

### 3. Implicit equation for the effective bond stretch

The thermodynamic requirement

$$\frac{\partial \hat{\psi}_R(\Lambda)}{\partial \lambda_b} = 0, \quad (2.5)$$

reflects the fact that the actual value of the effective bond stretch  $\lambda_b$  adopted by the material is the one that minimizes the free energy. This equation serves as an implicit equation to determine  $\lambda_b$  in terms of the other constitutive variables.

### 4. Microstresses $\varpi$ and $\xi$

The scalar microstress  $\varpi$  is given by

$$\varpi = \underbrace{\frac{\partial \hat{\psi}_R(\Lambda)}{\partial d}}_{\varpi_{en}} + \underbrace{\alpha + \zeta \dot{d}}_{\varpi_{diss}} \quad (2.6)$$

with  $\alpha = \hat{\alpha}(\Lambda)$  and  $\zeta = \hat{\zeta}(\Lambda)$  positive-valued scalar functions. Here  $\varpi_{en}$  and  $\varpi_{diss}$  denote the energetic and dissipative parts of  $\varpi$ .

The vector microstress  $\xi$  is given by,

$$\xi = \frac{\partial \hat{\psi}_R(\Lambda)}{\partial \nabla d}, \quad (2.7)$$

and is taken to be energetic, with no dissipative contribution.

<sup>2</sup> Notation: We use standard notation of modern continuum mechanics ([Gurtin et al., 2010](#)). Specifically:  $\nabla$  and  $\text{Div}$  denote the gradient and divergence with respect to the material point  $\mathbf{X}$  in the reference configuration, and  $\Delta = \text{Div} \nabla$  denotes the referential Laplace operator;  $\text{grad}$ ,  $\text{div}$ , and  $\text{div grad}$  denote these operators with respect to the point  $\mathbf{x} = \chi(\mathbf{X}, t)$  in the deformed body; a superposed dot denotes the material time-derivative. Throughout, we write  $\mathbf{F}^{e-1} = (\mathbf{F}^e)^{-1}$ ,  $\mathbf{F}^{e-\top} = (\mathbf{F}^e)^{-\top}$ , etc. We write  $\text{tr}\mathbf{A}$ ,  $\text{sym}\mathbf{A}$ ,  $\text{skw}\mathbf{A}$ ,  $\mathbf{A}_0$ , and  $\text{sym}_0\mathbf{A}$  respectively, for the trace, symmetric, skew, deviatoric, and symmetric-deviatoric parts of a tensor  $\mathbf{A}$ . Also, the inner product of tensors  $\mathbf{A}$  and  $\mathbf{B}$  is denoted by  $\mathbf{A} : \mathbf{B}$ , and the magnitude of  $\mathbf{A}$  by  $|\mathbf{A}| = \sqrt{\mathbf{A} : \mathbf{A}}$ .

## 2.2. Governing partial differential equations

The governing partial differential equations consist of

### 1. Equation of motion:

$$\text{Div} \mathbf{T}_R + \mathbf{b}_{0R} = \rho_R \ddot{\chi}, \quad (2.8)$$

where  $\mathbf{b}_{0R}$  is a non-inertial body force,  $\rho_R$  is the referential mass density,  $\ddot{\chi}$  the acceleration, and the Piola stress  $\mathbf{T}_R$  is given by (2.4). In the numerical simulations presented later in Sections 5 and 6, we neglect all inertial effects and body forces.

### 2. Microforce balance:

The microforces  $\varpi$  and  $\xi$  obey the balance (A.28), viz.

$$\text{Div} \xi - \varpi = 0. \quad (2.9)$$

This microforce balance, together with the thermodynamically consistent constitutive equations (2.6) and (2.7) for  $\varpi$  and  $\xi$  gives the following evolution equation for the damage variable  $d$ ,<sup>3</sup>

$$\hat{\zeta}(\Lambda)d = -\frac{\partial \hat{\psi}_R(\Lambda)}{\partial d} + \text{Div}\left(\frac{\partial \hat{\psi}_R(\Lambda)}{\partial \nabla d}\right) - \hat{\alpha}(\Lambda). \quad (2.10)$$

Since  $\zeta$  is positive-valued, the right hand side of (2.10) must be positive for  $\dot{d}$  to be positive and the damage to increase monotonically.

## 2.3. Boundary and initial conditions

We also need boundary and initial conditions to complete the theory.

### 1. Boundary conditions for the PDE governing the evolution of $\chi$ :

Let  $S_\chi$  and  $S_{t_R}$  be complementary subsurfaces of the boundary  $\partial B$  of the body  $B$ . Then for a time interval  $t \in [0, T]$  we consider a pair of boundary conditions in which the motion is specified on  $S_\chi$  and the surface traction on  $S_{t_R}$ :

$$\left. \begin{array}{l} \chi = \check{\chi} \quad \text{on } S_\chi \times [0, T], \\ \mathbf{T}_R \mathbf{n}_R = \check{\mathbf{t}}_R \quad \text{on } S_{t_R} \times [0, T]. \end{array} \right\} \quad (2.11)$$

In the boundary conditions above  $\check{\chi}$  and  $\check{\mathbf{t}}_R$  are prescribed functions of  $\mathbf{X}$  and  $t$ .

### 2. Boundary conditions for the PDE governing the evolution of $d$ :

The presence of microscopic stresses  $\xi$  results in an expenditure of power

$$\int_{\partial B} (\xi \cdot \mathbf{n}_R) \dot{d} \, da_R$$

by the material in contact with the body (cf., (A.29)), and this necessitates a consideration of boundary conditions on  $\partial B$  involving the microscopic tractions  $\xi \cdot \mathbf{n}_R$  and the rate of change of the damage variable  $\dot{d}$ .

- We restrict attention to boundary conditions that result in a null expenditure of microscopic power in the sense that  $(\xi \cdot \mathbf{n}_R) \dot{d} = 0$ .

A simple set of boundary conditions which satisfies this requirement is,

$$\left. \begin{array}{l} \dot{d} = 0 \quad \text{on } S_d \times [0, T], \\ \xi \cdot \mathbf{n}_R = 0 \quad \text{on } \partial B \setminus S_d \times [0, T], \end{array} \right. \quad (2.12)$$

with the microforce  $\xi$  given by (2.7).

The initial data is taken as

$$\chi(\mathbf{X}, 0) = \mathbf{X}, \quad \dot{\chi}(\mathbf{X}, 0) = \mathbf{v}_0(\mathbf{X}), \quad \text{and} \quad d(\mathbf{X}, 0) = 0. \quad \text{in } B. \quad (2.13)$$

The coupled set of equations (2.8) and (2.10) together with (2.11), (2.12), and (2.13) yield an initial/boundary-value problem for the motion  $\chi(\mathbf{X}, t)$ , and the damage variable  $d(\mathbf{X}, t)$ .

<sup>3</sup> We use the phrases “damage variable” and “phase-field” interchangeably to describe  $d$ .

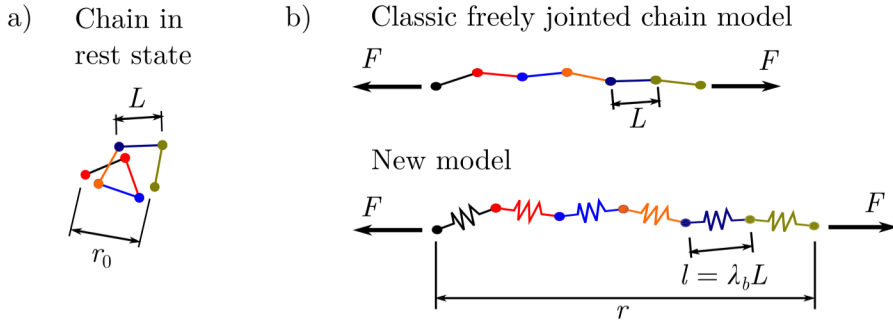


**Fig. 1.** a) Chain in the rest state. The Kuhn segment length in the rest state is  $L$ . b) Upper panel: classic freely jointed chain model under stretch. The Kuhn segments are assumed rigid. Bottom panel: model of Mao et al. (2017b). The Kuhn segments are assumed deformable due to deformation of the constituent bonds.

### 3. Specialization of the constitutive equations

As stated in the introduction, we wish to characterize the process of rupture in elastomeric material in terms of the microscopic mechanics of molecular bond scission between the backbone units of the polymer chains. However, the traditional hyperelastic models for elastomers neglect the energetics of bond deformation. In order to make this connection between the scales, we make use of our recently proposed hyperelastic constitutive model that accounts for the energetics of bond deformation, as well as the well-known entropic elasticity effects in polymers (Mao et al., 2017b). In what follows we begin by considering the process of deformation, damage, and rupture of a single chain, and then extend the single chain considerations to bulk elastomeric materials.

#### 3.1. Deformation, damage, and fracture of a single chain

##### 3.1.1. Free energy of a single chain in the absence of damage

To illustrate the model of Mao et al. (2017b) let us consider first the behavior of a single chain. We make the kinematic assumption that the overall deformation of the polymer chain under load is due to two sources: (i) the alignment of the Kuhn segments in the chain under load, and (ii) stretching of the segments due to deformation of the constituent molecular bonds (see Fig. 1).

Consider a single chain with  $n$  segments, each of initial length  $L$ , and as is standard, let  $r_0 = \sqrt{n}L$  denote the unstretched chain length determined from random-walk statistics. With  $r$  denoting the end-to-end distance of chain in a deformed configuration, let  $\lambda = r/r_0$  denote the overall chain stretch. The current segment length  $l$  is related to the rest length  $L$  through  $l = \lambda L_b$ , where  $\lambda_b$  is a dimensionless stretch which we refer to as the *bond stretch*. Using the Langevin statistics for the chain segments as developed in Kuhn and Grün (1942), the entropy of the chain is (Mao et al., 2017b),

$$\eta = \hat{\eta}(\lambda, \lambda_b) = -nk_B \left[ \frac{\lambda \lambda_b^{-1}}{\sqrt{n}} \beta + \ln \left( \frac{\beta}{\sinh \beta} \right) \right], \quad (3.1)$$

with

$$\beta = \mathcal{L}^{-1} \left( \frac{\lambda \lambda_b^{-1}}{\sqrt{n}} \right), \quad (3.2)$$

where  $\mathcal{L}^{-1}$  denotes the inverse of the Langevin function  $\mathcal{L}(x) = \coth x - x^{-1}$ , and  $k_B$  is Boltzmann's constant. Note from (3.1) and (3.2), that it is

the modified stretch measure ( $\lambda \lambda_b^{-1}$ ) which gives rise to changes in the entropy of the chain. (3.3)

We refer to ( $\lambda \lambda_b^{-1}$ ) as the *stretch due to segment realignment*.

Next, we consider how the deformation of the bonds causes the internal energy of the chain  $\varepsilon$  to change. In the following we use a simple functional form for the internal energy of the chain,

$$\varepsilon = \hat{\varepsilon}(\lambda_b) = \frac{1}{2} n E_b (\lambda_b - 1)^2, \quad (3.4)$$

where  $E_b$  is a parameter with units of energy that characterizes the bond stiffness.

The Helmholtz free energy density is defined as  $\psi = \varepsilon - \vartheta \eta$ , which, upon substituting the specialized constitutive equations (3.1) and (3.4) yields,

$$\psi = \hat{\psi}(\lambda, \lambda_b) = \frac{1}{2} n E_b (\lambda_b - 1)^2 + nk_B \vartheta \left[ \left( \frac{\lambda \lambda_b^{-1}}{\sqrt{n}} \right) \beta + \ln \left( \frac{\beta}{\sinh \beta} \right) \right]. \quad (3.5)$$

Next, to find  $\lambda_b$ , we use the fact that at fixed  $\lambda$ , a particular value of  $\lambda_b$  will minimize the free energy (cf., (2.5)), and this will be the most probable state in which to find the system. Thus,

$$\lambda_b = \arg \min_{\lambda_b^* > \lambda/\sqrt{n}} \hat{\psi}_R(\lambda, \lambda_b^*), \quad (3.6)$$

which provides an implicit, nonlinear equation to determine  $\lambda_b$ .

Note that in the classical freely jointed chain model there is no bond stretch, i.e.,  $\lambda_b = 1$ , and there is no internal energy contribution to the free energy  $\psi$ . In this case, as  $\lambda \rightarrow \sqrt{n}$  the entropy vanishes and the free energy diverges. In contrast, the bond deformation mechanism (3.4) in the free energy expression (3.5) ensures that the quantity  $(\lambda \lambda_b^{-1})$  is always less than  $\sqrt{n}$  and that the free energy remains finite.

### 3.1.2. Accounting for damage and scission of a single chain

For simplicity, we assume that thermal effects are negligible and that all bonds in the chain stretch uniformly, and eventually damage and fail under increasing stretch. The softening is due to the weakening of the molecular attraction between monomer units as they are separated. Thus, introducing a damage variable  $d \in [0, 1]$ , this assumption leads us to adopt the following functional form for the free energy of a single chain,

$$\hat{\psi}(\lambda, \lambda_b, d) = g(d)\hat{\varepsilon}^0(\lambda_b) - \vartheta \hat{\eta}(\lambda, \lambda_b), \quad (3.7)$$

where  $\hat{\varepsilon}^0(\lambda_b)$  is the internal energy of an *undamaged* chain, as given by (3.4), and the function  $g(d)$  is a monotonically decreasing *degradation function* with value,

$$g(0) = 1,$$

which produces the usual elastic behavior of the bonds in the intact state  $d = 0$ , and has a value

$$g(1) = 0,$$

to represent the fully damaged state. In other words, the degradation function describes the decreasing stiffness of the bonds under large stretches. Additionally, the degradation function is subject to the constraint

$$g'(1) = 0,$$

so that the thermodynamic driving force for damage  $\varpi_{en} = \partial \hat{\psi} / \partial d$  vanishes as the chain becomes fully damaged.<sup>4</sup> A widely-used degradation function is

$$g(d) = (1 - d)^2; \quad (3.8)$$

we adopt it here.<sup>5</sup>

Consistent with our treatment of the segments as having equal stretch, the total dissipation from scission is approximately the binding energy of the monomer units times the number of monomer units in the chain. To reflect this in the model, we set the rate-independent part  $\alpha$  of the dissipative microstress  $\varpi_{diss}$  to<sup>6</sup>

$$\alpha = n\varepsilon_b^f, \quad (3.9)$$

where  $\varepsilon_b^f$  is the binding energy between the monomer units.

In the present considerations for a single chain, where the  $\nabla d$  term does not come into play, the microforce balance (2.10) becomes

$$\zeta \dot{d} = -\frac{\partial \hat{\psi}(\lambda, \lambda_b, d)}{\partial d} - \alpha. \quad (3.10)$$

Let us consider the rate independent limit ( $\zeta = 0$ ). Then, inserting (3.7) and (3.8) into this balance, and using the fact that  $d$  lies in the range  $d \in [0, 1]$ , we have that

$$d = \begin{cases} 0, & \text{if } \hat{\varepsilon}(\lambda_b) \leq n\varepsilon_b^f/2, \\ 1 - \frac{n\varepsilon_b^f/2}{\hat{\varepsilon}^0(\lambda_b)} & \text{if } \hat{\varepsilon}(\lambda_b) > n\varepsilon_b^f/2. \end{cases} \quad (3.11)$$

The bond stretch  $\lambda_b$  is determined implicitly by (2.5), which yields the nonlinear equation

$$(1 - d)^2 E_b(\lambda_b - 1) - k_B \vartheta \frac{\lambda}{\sqrt{n} \lambda_b^2} \mathcal{L}^{-1} \left( \frac{\lambda \lambda_b^{-1}}{\sqrt{n}} \right) = 0. \quad (3.12)$$

<sup>4</sup> Cf. Eq. (2.6) for definition  $\varpi_{en}$ .

<sup>5</sup> In our numerical calculations the degradation function is modified as

$$g(d) = (1 - d)^2 + k,$$

where  $k$  is a small, positive-valued constant, which is introduced to prevent ill-conditioning of the model when  $d = 1$ .

<sup>6</sup> cf. Eq. (2.6) for the definition  $\varpi_{diss}$ .

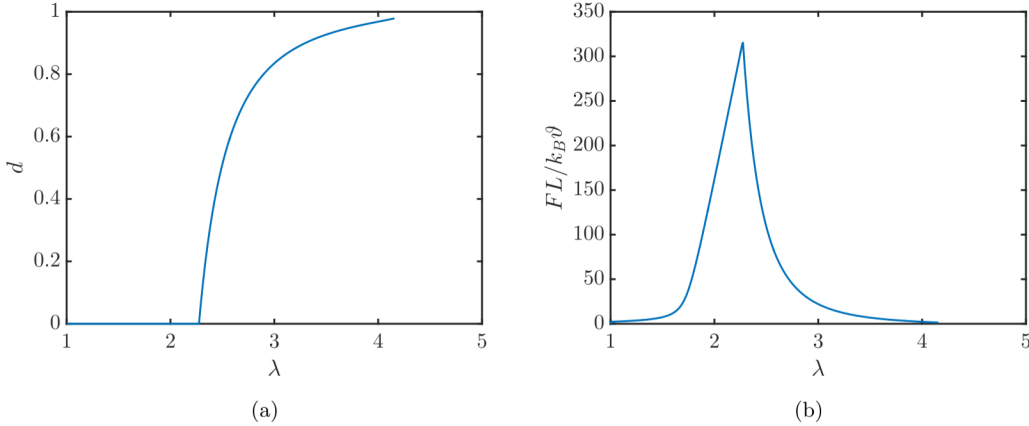


**Fig. 2.** Single chain response. (a) Evolution of the damage variable  $d$  with chain stretch  $\lambda$ . (b) Normalized chain force  $FL/k_B\vartheta$  versus chain stretch.

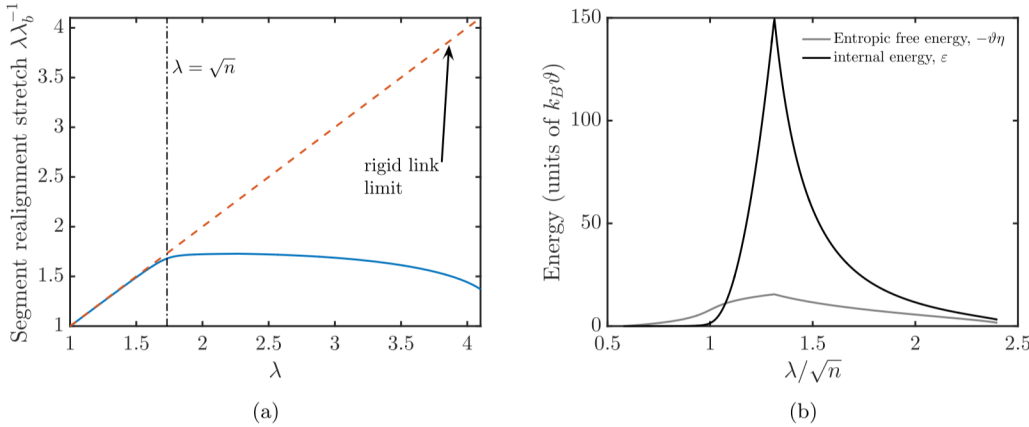


**Fig. 3.** Single chain model response. (a) Evolution of entropic stretch ( $\lambda\lambda_b^{-1}$  with chain stretch  $\lambda$ ). (b) Variation of the contributions ( $-\vartheta\eta$ ) and  $\varepsilon$  to the free energy with chain stretch.

Given an imposed chain stretch  $\lambda$ , Eqs. (3.11) and (3.12) can be solved simultaneously for  $d$  and  $\lambda_b$ .

We may visualize the behavior of the model with the following simple example, in which we take

$$n = 3, \quad E_b/k_B\vartheta = 1000, \quad \varepsilon_b^f/k_B\vartheta = 100,$$

and impose a monotonically increasing stretch and sketch the resulting response.<sup>7</sup> The evolution of the damage variable  $d$  is plotted against the imposed stretch  $\lambda$  in Fig. 2a. The damage variable  $d$  remains zero until the internal energy reaches the critical value  $\varepsilon_b^f/2$  (which occurs at  $\lambda \approx 2.3$ ). After reaching this point, the damage variable increases and asymptotically approaches unity according to (3.11). In Fig. 2b, the chain force  $F$  (presented in the dimensionless form  $FL/k_B\vartheta = (\sqrt{nk_B\vartheta})^{-1}\partial\hat{\psi}/\partial\lambda$ ) is plotted against the imposed stretch  $\lambda$ . The force follows the undamaged stiffening response until the critical value of the internal energy is reached. At that point, the damage variable begins to increase according to (3.11), and the bond stiffness begins to degrade, leading to a decrease in force with increasing stretch.

Next, we illustrate the deformation mechanisms in the model. Recall from (3.3) that the stretch measure ( $\lambda\lambda_b^{-1}$ ) gives rise to the change in the entropy of the chain. Fig. 3a shows a plot of  $\lambda\lambda_b^{-1}$  against the imposed stretch  $\lambda$ . When the imposed stretch is below  $\sqrt{n}$  (the limiting stretch in the classical freely jointed chain model), the overall chain stretch and the stretch due to segment realignment are virtually identical. In other words, the behavior of the chain in this range is virtually identical to the classic freely jointed chain model, which has perfectly rigid links. Since the bonds are quite stiff in this example ( $E_b/k_B\vartheta = 1000$ ), it is energetically favorable for the system to accommodate stretch primarily through the entropic mechanism when  $\lambda < \sqrt{n}$ . This is further demonstrated in Fig. 3b, where both components of the free energy, entropic ( $-\vartheta\eta$ ) and the internal energy ( $\varepsilon$ ), are plotted. The internal energy due to bond stretching is seen to be negligible until  $\lambda \approx \sqrt{n}$ . On the other hand, as the stretch passes  $\sqrt{n}$ , the chain approaches its contour length, the configurational entropy is nearly exhausted, and it becomes energetically favorable to accommodate additional stretch through bond deformation. Thus, the realignment stretch ( $\lambda\lambda_b^{-1}$ ) remains approximately constant as the overall stretch  $\lambda$  increases beyond  $\sqrt{n}$  in Fig. 3a.

<sup>7</sup> We have intentionally chosen a small value  $n = 3$  for the number of links in the chain to illustrate the features of our theory so that failure of the chains in our simulations occurs at reasonable levels of stretch  $\lambda$ .

The next major event occurs when the bonds reach the critical energy for softening to begin ( $\lambda \approx 2.3 \approx 1.3\sqrt{n}$ ). To visualize the response, one may imagine the system as a mechanical model of two springs in series, one representing the entropic elasticity, and the other representing the energetic elasticity. The parameter  $(1-d)^2 E_b$  can be considered the effective stiffness of the energetic elasticity spring. As the damage variable increases,  $(1-d)^2 E_b$  decreases, and the stretch of the energetic spring increases at the expense of the stretch in the entropic spring. In other words, the bond stretch  $\lambda_b$  increases and the segment realignment stretch  $(\lambda\lambda_b^{-1})$  decreases once damage begins, as seen in Fig. 3a. It follows that during damage, the entropy begins to increase. This is expected, as the length of the Kuhn segments is rapidly increasing, and with longer Kuhn segments there are a greater number of configurations possible to achieve the overall stretch.

**Remark.** The microforce balance (3.10) can be rewritten to enforce the constraint  $d \in [0, 1]$ , which leads to (3.11) in a simple way. To find it, first substitute (3.7), (3.8), and (3.9) into the microforce balance (3.10), and then add and subtract the term  $n\varepsilon_b^f d$  to get

$$\zeta \dot{d} = 2(1-d)(\hat{\varepsilon}^0(\lambda_b) - n\varepsilon_b^f/2) - n\varepsilon_b^f d.$$

The constraint is automatically satisfied if the equation above is modified to read as,

$$\zeta \dot{d} = 2(1-d)\langle \hat{\varepsilon}^0(\lambda_b) - n\varepsilon_b^f/2 \rangle - n\varepsilon_b^f d, \quad (3.13)$$

where  $\langle \cdot \rangle$  are Macauley brackets, i.e.,

$$\langle x \rangle = \begin{cases} 0, & x < 0, \\ x, & x \geq 0. \end{cases}$$

In this form, a threshold for the damage driving force is made explicit.

### 3.2. Deformation, damage, and fracture of a network of chains

We employ the widely-used eight-chain network representation of Arruda and Boyce (1993) to extend the single chain model to a continuum model.<sup>8</sup> The entropy and energy of the network can be obtained by summing the contributions from individual chains as given by the single chain model. To this end, we follow Anand (1996) and define the effective chain stretch

$$\bar{\lambda} \stackrel{\text{def}}{=} \sqrt{\text{tr}\bar{\mathbf{C}}/3}, \quad (3.14)$$

where  $\bar{\mathbf{C}}$  is the distortional right Cauchy-Green tensor. With  $N$  representing the number of chains per unit volume of the reference configuration, the entropy density of the network is then given by

$$\eta_R = \hat{\eta}_R(\bar{\lambda}, \lambda_b) = -Nk_B n \left[ \left( \frac{\bar{\lambda}\lambda_b^{-1}}{\sqrt{n}} \right) \beta + \ln \left( \frac{\beta}{\sinh \beta} \right) \right], \quad \beta = \mathcal{L}^{-1} \left( \frac{\bar{\lambda}\lambda_b^{-1}}{\sqrt{n}} \right). \quad (3.15)$$

For the internal energy density of a network we allow for a dependence on  $\lambda_b$  and  $d$  as in our consideration for a single chain, but here we also allow for internal energy contribution due to volumetric changes,  $J$ , and also a dependence on the gradient of the damage,  $\nabla d$ :

$$\varepsilon_R = \hat{\varepsilon}_R(\lambda_b, J, d, \nabla d) = g(d)\hat{\varepsilon}_R^0(\lambda_b, J) + \hat{\varepsilon}_{R,\text{nonloc}}(\nabla d). \quad (3.16)$$

For the undamaged part of the internal energy  $\hat{\varepsilon}_R^0(\lambda_b, J)$  we choose the constitutive relation

$$\hat{\varepsilon}_R^0(\lambda_b, J) = \frac{1}{2} N n E_b (\lambda_b - 1)^2 + \underbrace{\frac{1}{2} K (J - 1)^2}_{\hat{\varepsilon}_{Rv}(J)}, \quad (3.17)$$

where the first term represents the internal energy of bond stretching, and the second term models the slight compressibility of the material, with  $K$  a bulk modulus.<sup>9</sup>

<sup>8</sup> Note that in addition to the usual assumption of weak chain interactions, we must additionally assume that the damage in each chain is independent in order apply the Arruda-Boyce network model.

<sup>9</sup> The particular form of the volumetric internal energy is not crucial for elastomers in which the volume changes are typically quite small relative to distortional deformations. In our finite element simulations we encountered some convergence difficulties with the simple quadratic form,  $\hat{\varepsilon}_{Rv}(J) = 1/2K(J - 1)^2$ , of the volumetric internal energy at late stages of the damage. Accordingly, in our computations we have used the alternate form  $\hat{\varepsilon}_{Rv}(J) = K/8(J - J^{-1})^2$  which reduces to a simple quadratic energy as  $J \rightarrow 1$ .

$$\hat{\varepsilon}_{Rv}(J) = \frac{K}{8} (J - J^{-1})^2 = \frac{K}{8} (J - 1)^2 \left( 1 + \frac{1}{J} \right)^2 \approx \frac{1}{2} K (J - 1)^2.$$

If for some numerical reason  $J$  becomes large during the iteration process, then the alternate form leads to a softer response (see Schröder and Neff, 2003).

The term  $\hat{\varepsilon}_{R,\text{nonloc}}(\nabla d)$  in the internal energy density is the nonlocal contribution

$$\hat{\varepsilon}_{R,\text{nonloc}}(\nabla d) = \frac{1}{2} \varepsilon_R^f \ell^2 |\nabla d|^2, \quad (3.18)$$

where  $\ell$  represents an intrinsic length scale for the damage process, and

$$\varepsilon_R^f \stackrel{\text{def}}{=} N n \varepsilon_b^f. \quad (3.19)$$

represents the energy of chain scission per unit volume when all bonds are broken. In formulating a theory that accounts for the stretching and failure of the Khun segments, [Mao et al. \(2017b\)](#) assumed that all Khun segments are uniformly stretched and that they fail simultaneously. This is a significant assumption, since the chain is subject to thermal fluctuations, and one expects this to lead to failure at a single bond. We neglect this complication to construct a simple and tractable model, and argue for its plausibility on the grounds that the binding energy of backbone units of typical polymers is large in comparison to the average thermal energy at room temperature.

**Remark.** A macroscopic critical energy release rate  $G_c$  can be estimated for the case of strongly crosslinked elastomers. In this case the internal energy will significantly outweigh the entropic free energy at the point of scission, and thus the entropic free energy contribution to the energy release rate is negligible. In the gradient-damage model, the dissipation scales as  $\varepsilon_R^f \ell^3$ , while for a theoretical sharp crack it would scale as  $G_c \ell^2$ , so that

$$\varepsilon_R^f \times \ell \approx G_c.$$

With the constitutive relations (3.15)-(3.19) for  $\varepsilon_R$  and  $\eta_R$  in hand, the free energy  $\psi_R$  follows from the definition

$$\psi_R = \varepsilon_R - \vartheta \eta_R. \quad (3.20)$$

To complete the specification of the constitutive relations, we specify the dissipative microforce  $\varpi_{\text{diss}}$  that expends power through  $d$ .<sup>10</sup> The dissipative microforce is partitioned into a rate independent part and a rate dependent part through

$$\varpi_{\text{diss}} = \underbrace{\alpha}_{\text{rate-independent}} + \underbrace{\zeta \dot{d}}_{\text{rate-dependent}}. \quad (3.21)$$

The rate-independent part of the dissipative microforce  $\alpha$  is the sum of the contributions from each chain and given by (3.19), thus

$$\alpha = \varepsilon_R^f. \quad (3.22)$$

The rate-dependent contribution to the dissipative microforce  $\zeta \dot{d}$ , is simply described by a constant kinetic modulus  $\zeta > 0$ , with the rate-independent limit of damage evolution given by  $\zeta \rightarrow 0$ .

Using the specializations above, the microforce balance (2.10), which gives the evolution of  $d$ , becomes

$$\zeta \dot{d} = 2(1-d)\hat{\varepsilon}_R^0(\lambda_b, J) + \varepsilon_R^f \ell^2 \Delta d - \varepsilon_R^f. \quad (3.23)$$

Keeping in mind the threshold for damage initiation (3.11), and to make connection with the previous work of Miehe and co-workers (cf., e.g., [Miehe et al., 2010b](#); [Miehe and Schänel, 2014](#)), we apply the same technique used in (3.13) to rewrite the evolution Eq. (3.23) as

$$\zeta \dot{d} = 2(1-d)\langle \hat{\varepsilon}_R^0(\lambda_b, J) - \varepsilon_R^f/2 \rangle - \varepsilon_R^f(d - \ell^2 \Delta d). \quad (3.24)$$

At this stage, the irreversible nature of scission is not yet reflected in the model. To this end, we replace the term  $\langle \hat{\varepsilon}_R^0(\lambda_b, J) - \varepsilon_R^f/2 \rangle$  in the microforce balance with the monotonically increasing history field function (cf., [Miehe et al., 2010b](#)):

$$\mathcal{H}(t) \stackrel{\text{def}}{=} \max_{s \in [0,t]} \langle \hat{\varepsilon}_R^0(\lambda_b(s), J(s)) - \varepsilon_R^f/2 \rangle. \quad (3.25)$$

The microforce balance (2.10) then becomes

$$\zeta \dot{d} = 2(1-d)\mathcal{H} - \varepsilon_R^f(d - \ell^2 \Delta d). \quad (3.26)$$

**Remark.** The structure of our theory is similar in many respects to phase-field models of fracture based on the top-down, critical energy release rate approach for polymers (cf., e.g., [Miehe and Schänel, 2014](#); [Wu et al., 2016](#)) and [Raina and Miehe \(2016\)](#). A reader familiar with these works might expect to see the degradation function  $g(d)$  multiplying the entire undamaged free energy

$$g(d) \underbrace{(\varepsilon_R^0 - \vartheta \eta_R)}_{\psi_R^0}, \quad (3.27)$$

instead of degrading only the internal energy as in (3.16). This choice would induce a *free energy of scission* as a material parameter instead of the internal energy of scission,  $\varepsilon_R^f$ , appearing in our theory. The advantage of our proposed form is that it respects the energetics of molecular bond dissociation.

<sup>10</sup> Cf. eq. (2.7).

#### 4. Summary of the governing partial differential equations for the specialized theory

##### 1. Balance of forces:

We neglect all body forces and inertial effects, and take balance of forces in the referential form,

$$\text{Div}\mathbf{T}_R = \mathbf{0}, \quad (4.1)$$

with  $\mathbf{T}_R$  given by

$$\mathbf{T}_R = \tilde{G} (J^{-2/3} \mathbf{F} - \bar{\lambda}^2 \mathbf{F}^{-\top}) + (1-d)^2 K (J-1) J \mathbf{F}^{-\top}, \quad (4.2)$$

where

$$\tilde{G} \stackrel{\text{def}}{=} G_0 \left( \frac{1}{3} \frac{\sqrt{n}}{\bar{\lambda} \lambda_b} \right) \mathcal{L}^{-1} \left( \frac{\bar{\lambda} \lambda_b^{-1}}{\sqrt{n}} \right) \quad \text{with} \quad G_0 = N k_B \vartheta, \quad (4.3)$$

is a generalized shear modulus in which the effective stretch is  $\bar{\lambda} = \sqrt{\bar{C}/3}$ , and the effective bond stretch  $\lambda_b$  is determined by solving the implicit equation

$$(1-d)^2 E_b (\lambda_b - 1) - k_B \vartheta \left( \frac{\bar{\lambda}}{\sqrt{n} \lambda_b^2} \right) \mathcal{L}^{-1} \left( \frac{\bar{\lambda} \lambda_b^{-1}}{\sqrt{n}} \right) = 0. \quad (4.4)$$

Here,  $\mathcal{L}^{-1}$  is the inverse of the Langevin function  $\mathcal{L}(x) = \coth x - x^{-1}$ . Note that generalized shear modulus  $\tilde{G}$  is connected to the damage field  $d$  implicitly through Eq. (4.4) for  $\lambda_b$ .

##### 2. Microforce balance. Non-local evolution equation for $d$ :

$$\zeta \dot{d} = 2(1-d)\mathcal{H} - \varepsilon_R^f (d - \ell^2 \Delta d), \quad (4.5)$$

with

$$\varepsilon_R^f = N n \varepsilon_b^f, \quad (4.6)$$

a fracture energy, and a history field function  $\mathcal{H}$  defined by

$$\mathcal{H}(t) \stackrel{\text{def}}{=} \max_{s \in [0,t]} \langle \hat{\varepsilon}_R^0(\lambda_b(s), J(s)) - \varepsilon_R^f / 2 \rangle, \quad (4.7)$$

where at each  $s \in [0, t]$ ,

$$\hat{\varepsilon}_R^0(\lambda_b(s), J(s)) = \frac{1}{2} N n E_b (\lambda_b(s) - 1)^2 + \frac{1}{2} K (J(s) - 1)^2. \quad (4.8)$$

The boundary conditions for these partial differential equations have been discussed previously in Section 2.3.

The theory involves the following material parameters:

$$N, \quad n, \quad E_b, \quad K, \quad \varepsilon_b^f, \quad \ell, \quad \text{and} \quad \zeta. \quad (4.9)$$

Here,  $N$  is the number of chains per unit volume;  $n$  is the number of Kuhn segments in a chain;  $E_b$  represents the modulus related to stretching of the bonds (Kuhn segments) of the polymer molecules;  $K$  represents the bulk modulus of the material;  $\varepsilon_b^f$ , a bond dissociation energy per unit volume;  $\ell$  is a characteristic length scale of the gradient theory under consideration; and  $\zeta$  is a kinetic modulus for the evolution of the damage. All parameters are required to be positive.

In the numerical simulations described in the next two sections, instead of the parameter list (4.9), we use the parameter list,

$$G_0 = N k_B \vartheta, \quad n, \quad \bar{E}_b = N n E_b, \quad K, \quad \varepsilon_R^f = N n \varepsilon_b^f, \quad \ell, \quad \text{and} \quad \zeta. \quad (4.10)$$

where  $G_0$  is the ground-state shear modulus for the polymer network,  $\bar{E}_b$  is a bond-stiffness parameter for the network, and  $\varepsilon_R^f$  represents the energy per unit volume for the dissociation of all the Kuhn segments in a network.

**Remark.** In our gradient-damage theory the free energy has a contribution (3.18) in which  $\varepsilon_R^f$  represents the energy of chain scission per unit volume, and  $\ell$  is a length scale to account for gradient effects in the damage field  $d$ . Theoretically,  $\ell$  is an intrinsic material parameter of the theory. Actual values of  $\ell$  in elastomeric materials are expected to be  $\ell \lesssim 1 \mu\text{m}$ . For such a value of  $\ell$ , to numerically resolve regions of sharp gradients in the damage variable  $d$ , the finite element size  $h_e$  must be much smaller than  $\ell$  — typically  $h_e \lesssim \ell/10$  — so that  $h_e \lesssim 100 \text{ nm}$ , which is *exceedingly small*. Use of such a small element size in the damage zone is computationally tractable (on our computers) if the in-plane dimensions of a single-edge-notched specimen are less than 1 mm, and an edge crack is a few microns in size. Calculations for small specimens are shown in Section 5.

However, if one is interested in simulating the fracture of specimens which have a macroscopic in-plane dimensions of say 10 mm or larger, then use of such a small value of  $\ell$  and therefore a small value of  $h_e$ , will result in prohibitively expensive simulations. Under these circumstances, for pragmatic reasons,  $\ell$  may be considered a regularization parameter for

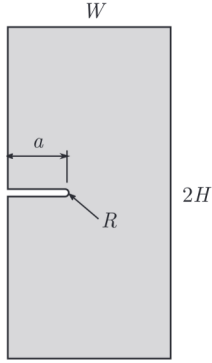


**Fig. 4.** Geometric parameters defining a single-edge-notched specimen (not to scale). We take  $W = 10a$  and  $H = 20a$ , and  $R$  is the root-radius of the notch.

**Table 1**

Material properties for the single-edge-notch simulations.

$G_0 = Nk_B\vartheta$	$n$	$\bar{E}_b = NnE_b$	$K$	$\varepsilon_R^f = Nn\varepsilon_b^f$	$\ell$	$\zeta$
0.25 MPa	4	500 MPa	625 MPa	25 MJ/m <sup>3</sup>	1 μm	50 MPa·s

the gradient-damage theory. Corresponding to a small but computationally-tractable mesh size  $h_e$  selected for macroscopic-dimensioned specimens, a suitably large value of  $\ell$  may be chosen, and the value of  $\varepsilon_R^f$  suitable reduced so that  $\varepsilon_R^f \times \ell \approx G_c$ , where  $G_c$  is the value of experimentally-measured macroscopic critical energy release rate for a given material. Calculations for large specimens are shown in Section 6. For the simulations of double-edge-notched thin sheets in tension shown in this section, a typical mesh that we used is displayed in Fig. 11 in Appendix C.

## 5. Application of the model to study flaw-sensitivity in elastomers

We demonstrate the behavior of the full nonlocal network model through an example. To this end, we apply the model to the problem of plane-stress Mode-I loading of a single-edge-notched specimen (see Fig. 4). The proposed model is implemented in the commercial finite element code Abaqus (Dassault Systèmes, v. 6.14) by writing our own user-defined elements. A brief description of the implementation is given in Appendix B.

The material properties used in our simulations are given in Table 1. The parameters  $G_0$ ,  $n$ , and  $K$  approximate those of a well cross-linked engineering elastomer. The values of the parameters  $\bar{E}_b$  and  $\varepsilon_R^f$  are in line with the estimates made in Mao et al. (2017b), and the length scale is set at  $\ell = 1\mu\text{m}$ . The kinetic modulus  $\zeta$  was chosen through trial-and-error so that it has only a minor effect on the load-displacement curves in the simulations.

We consider a series of geometries of different size that are each pre-notched to 10% of the specimen width. Referring to Fig. 4, each specimen is defined by the in-plane width  $W$ , half-height  $H$ , notch-depth  $a$ , and notch-root-radius  $R$ . We examine the case of flaws that are small enough to allow the material to stiffen significantly due to chain straightening before rupture occurs. The notch lengths considered are,

$$a = \{0.5 \mu\text{m}, 1 \mu\text{m}, 5 \mu\text{m}, 10 \mu\text{m}\}, \quad (5.1)$$

which when normalized by the length scale  $\ell = 1\mu\text{m}$  are,

$$a/\ell = \{0.5, 1, 5, 10\}.$$

We set the notch-root radius to be  $R = 1\mu\text{m}$  for all geometries. For each notch-length  $a$ , we take  $W = 10a$  and  $2H = 40a$ . The geometries thus range from 5 μm wide by 20μm high ( $a/\ell = 0.5$ ) to 100 μm by 400 μm ( $a/\ell = 10$ ). Note that there is not perfect similarity between the geometries, since the notch radius is kept fixed at 1μm in all cases. Each specimen is pulled in uniaxial tension at a nominal stretch rate of  $1 \times 10^{-2} \text{ s}^{-1}$ .

Fig. 5 shows the result from our simulation for a notch with  $a/\ell = 1$ . The nominal stress, normalized by  $G_0 = Nk_B\vartheta$ , versus nominal stretch curve is shown in Fig. 5(i), and Fig. 5(ii) shows the deformed geometry at points (a) through (g) on the stress-stretch curve, together with contours of the damage variable  $d$ . The image (a) in Fig. 5(ii) is the initial configuration. As the sample is stretched to point (b) the notch is blunted, but no damage has initiated. Damage initiates when the sample is stretched further to a stretch level of  $\sim 3.5$  (a point just before (c)), but the force is still increasing, and it is after additional macroscopic stretching that the force reaches a peak at point (d) in the stress-stretch curve, and from the contour of damage shown in Fig. 5(ii) (d), the damage zone ahead of the crack becomes clearly observable. Further stretching begins the rupture process, and Figs. 5(ii) (e) through (g) show this progressive rupturing, with (g) showing the final failed configuration.

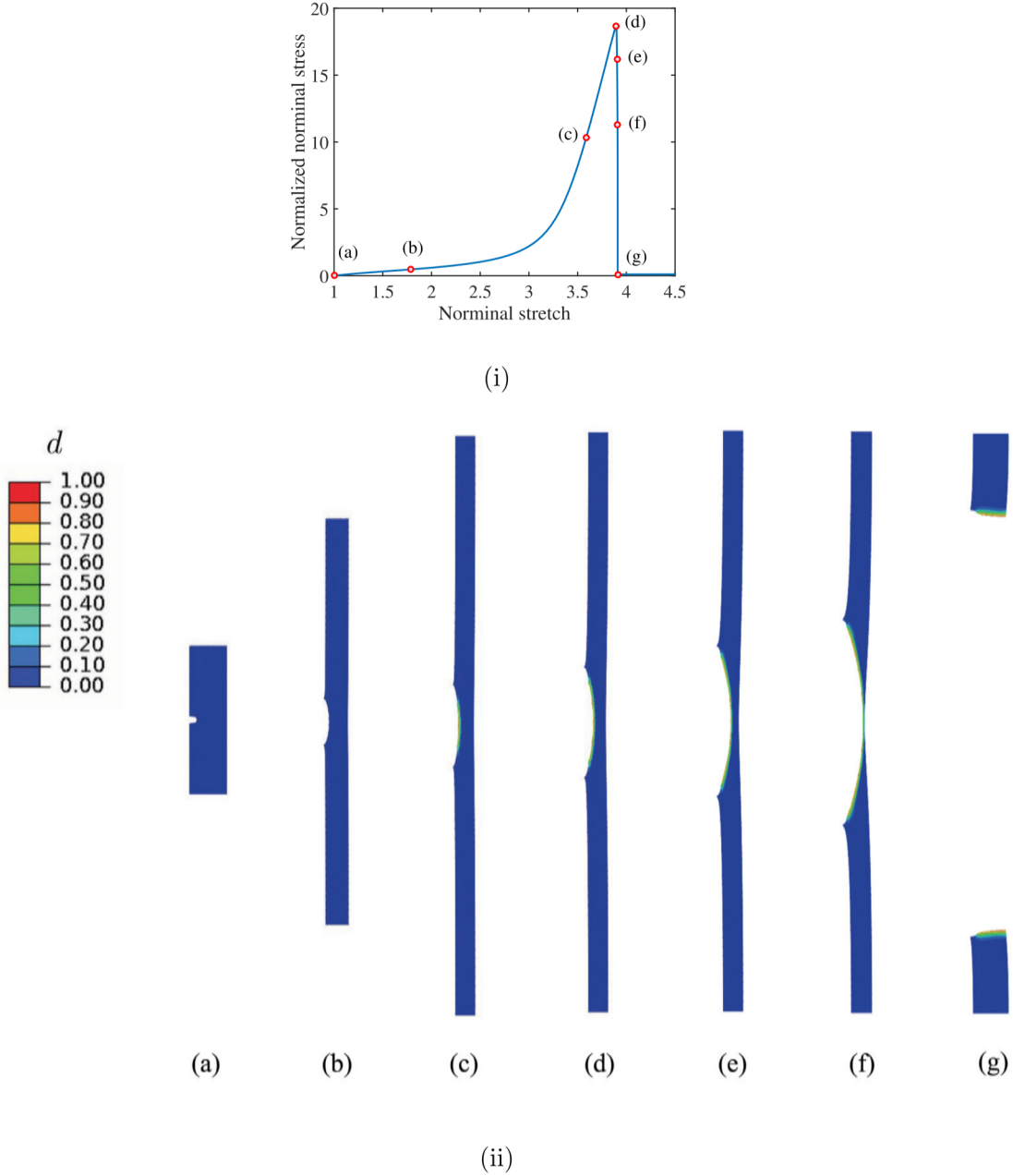
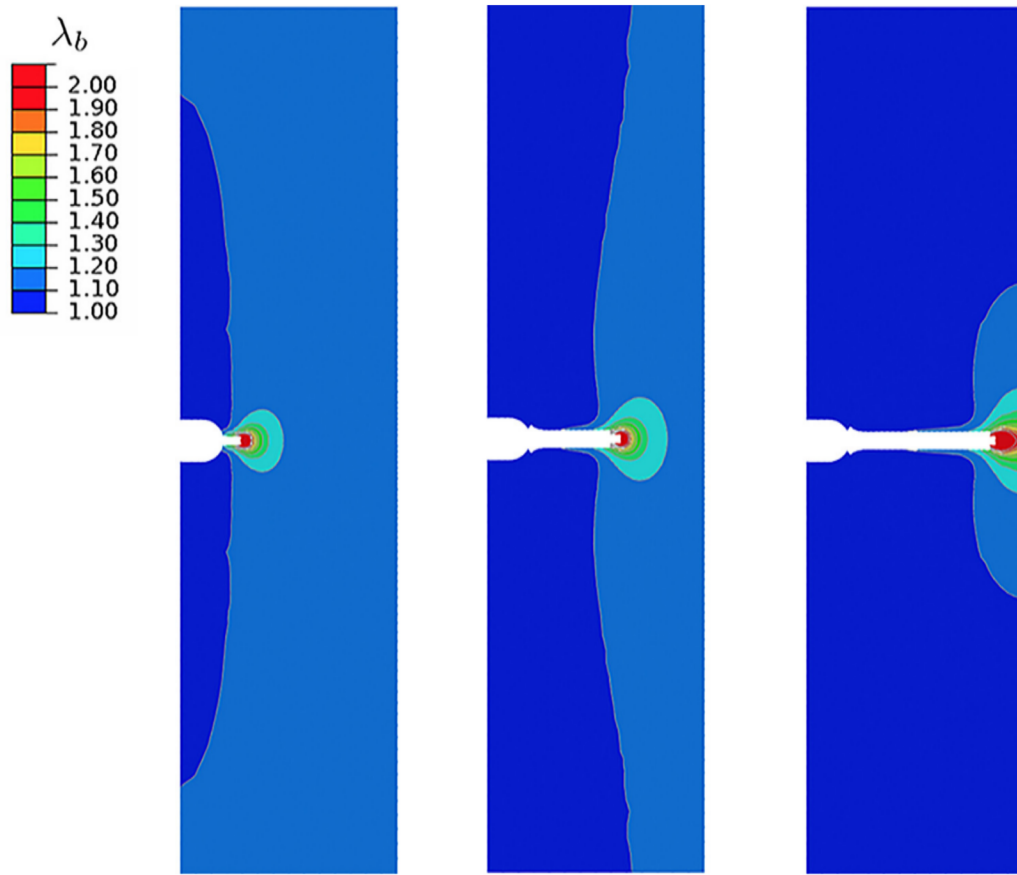


**Fig. 5.** Progressive damage and rupture for the case  $a/\ell = 1$ . (i) Computed nominal stress, normalized by  $G_0 = Nk_B\vartheta$ , versus nominal stretch curve. (ii) Deformed configurations of the specimen with contours of the damage variable  $d$  at points (a) through (g) in the stress-stretch curve. To aid visualization of the damage, elements with an average value of  $d > 0.95$  are removed from the plots.

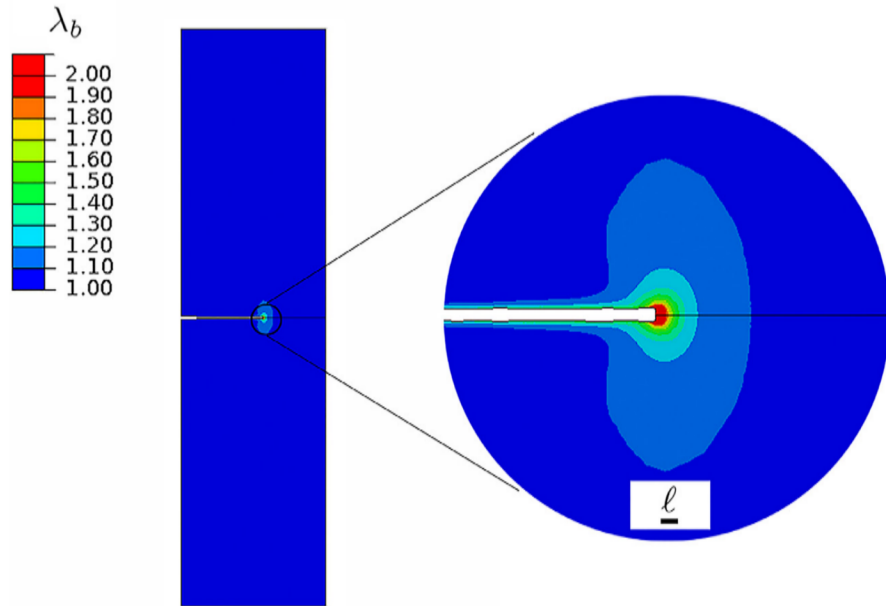
Next, we examine the role of the bond stretching on the overall response. In Figs. 6 and 7, we plot contours of the bond stretch  $\lambda_b$  during the deformation process. Highly damaged elements ( $d > 0.95$ ) are again hidden from view. The contours are plotted on the reference configuration to highlight the extent of crack propagation, relative to the initial specimen geometry.

Fig. 6 shows the bond deformation for a small flaw,  $a/\ell = 1$ . The image in the first frame is taken when extension of the notch has proceeded a small amount, while that in the last frame is just before final rupture of the specimen. The contour levels of  $\lambda_b$  show that there is appreciable bond-stretch in the entire specimen. The overall response is strongly influenced by the mechanics of bond-stretching, and the stress-bearing capacity of the material is being used efficiently.

A contour plot for  $\lambda_b$  for a specimen with a large flaw,  $a/\ell = 10$ , is shown in Fig. 7; the crack has propagated halfway through the specimen. In this case bond-stretching is limited to a small region in the vicinity of the crack tip; the majority of the specimen displays negligible bond-stretching, and that part of the specimen is thus well described by the Arruda-Boyce model without bond-stretching. This plot illustrates a case where the damage process zone at the crack-tip is small compared with the other in-plane dimensions of the specimen. For such circumstances a traditional top-down fracture mechanics approach based on the critical energy release rate may be applied, *but we do pursue such an approach here*.



**Fig. 6.** Contours of bond stretch  $\lambda_b$  during the fracture process for a notch with  $a/\ell = 1$ . Significant bond deformation occurs throughout the entire specimen. Snapshots are shown at three different stages of crack propagation. Contours are plotted on the reference configuration. Elements are removed from the figures when  $d > 0.95$ .



**Fig. 7.** Contours of bond stretch  $\lambda_b$  during the fracture process for a notch with  $a/\ell = 10$ . The bond stretch is appreciable only in a small process zone near the crack tip. Contours are plotted on the reference configuration. Elements are removed from the figures when  $d > 0.95$ .

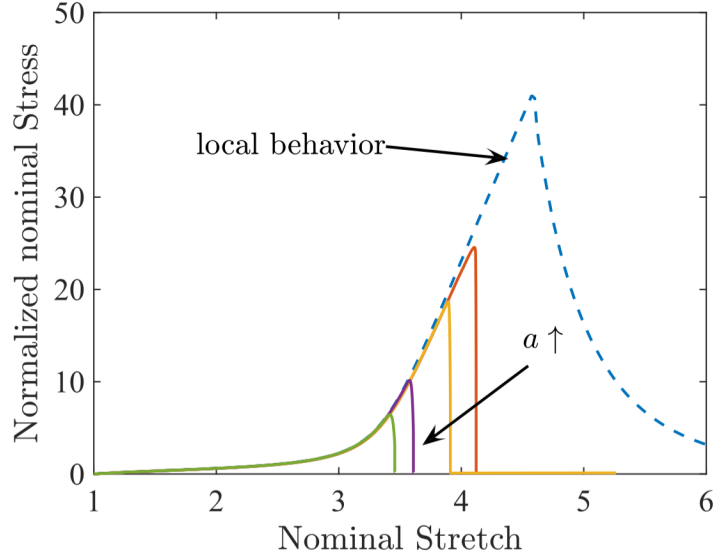


**Fig. 8.** Nominal stress, normalized by  $G_0 = Nk_B\vartheta$ , versus nominal stretch for all single-edge-notched geometries, with  $a/\ell = \{0.5, 1, 5, 10\}$  (solid lines). The dashed curve shows the local behavior of the model, representative of a homogeneous deformation state.

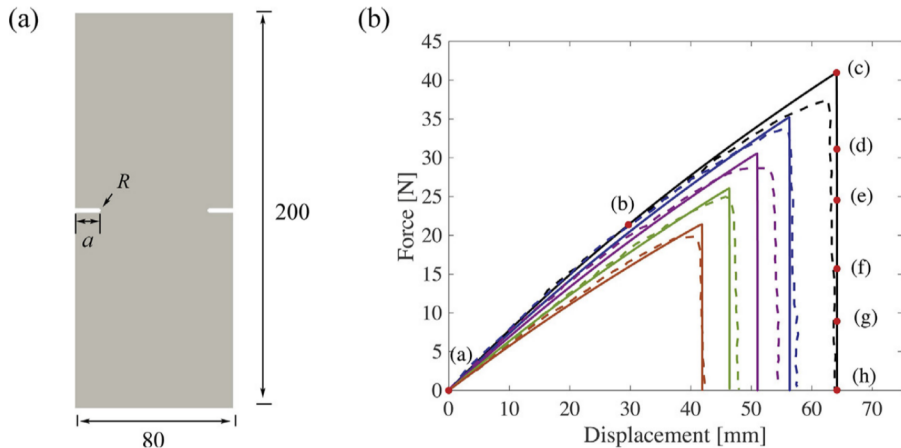


**Fig. 9.** Double-edge-notched specimen in tension. (a) Geometry of the specimen in mm, with different initial notch lengths  $a = \{12, 16, 20, 24, 28\}$  mm. The root-radius of the notch is fixed at  $R = 1$  mm (b). Comparison of load-deflection curves from simulations (solid-lines) against the experimental results of Hocine et al. (2002) (dashed-lines).

The normalized nominal stress versus nominal stretch response for all the geometries  $a/\ell = \{0.5, 1, 5, 10\}$  is shown in Fig. 8. For comparison, the ideal behavior of the material with no flaw is included on the plot as a dashed curve.<sup>11</sup> As the notch size decreases, the body approaches the strength of the local response. Note also that the gradual failure that occurs in the local response becomes a sudden event in the boundary value problem. This is indicative of the nonlocal behavior, with energy remote from the crack-tip being released to extend the crack.

## 6. Double-edge-notched thin sheets in tension

In the previous Section 5 we studied the capability of the model to describe flaw-size sensitivity in single-edge-notched specimens which are sub-millimeter in size, with micron-dimensional cracks. In this section we show the capability of our theory and numerical simulation capability to model the experimental results of Hocine et al. (2002) on fracture of double-edge-notched specimens of a styrene-butadiene elastomer (SBR) – specimens which are tens of millimeters in size, with millimeter-dimensional cracks.

Fig. 9(a) shows a schematic of the specimen geometry in the experiments of Hocine et al. (2002). The overall size of a notched sheet sample is 80 mm × 200 mm in the plane, and the sheet is 3 mm thick. We consider specimens with notch lengths  $a = 12, 16, 20, 24$ , and 28 mm; the initial root-radius of the notch is fixed at  $R = 1$  mm. The displacement of the

<sup>11</sup> The ideal behavior is computed by applying a uniaxial, plane stress deformation to a single material point, neglecting the nonlocal  $\nabla d$  term.

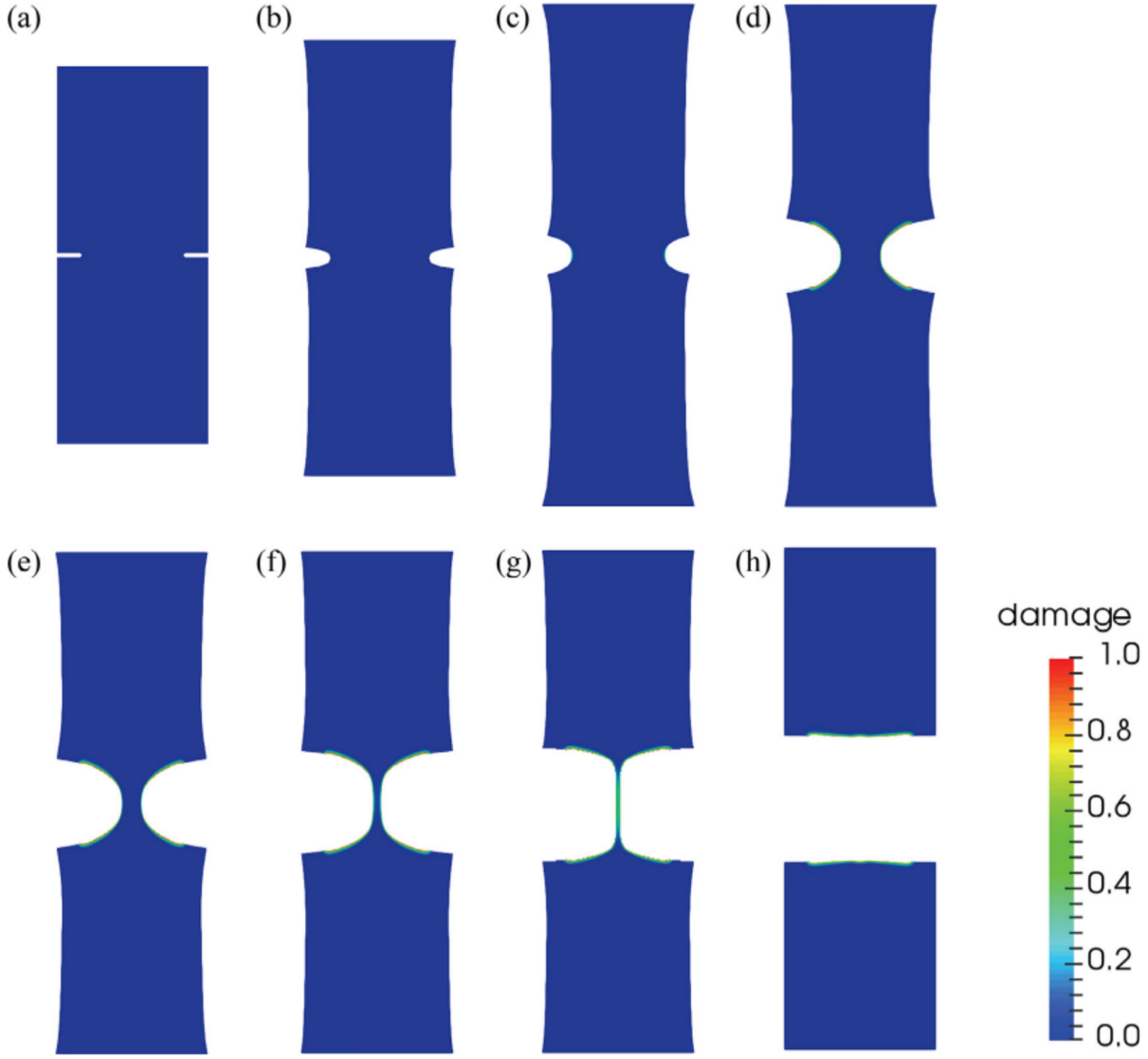


**Fig. 10.** Images of the deformed geometry with contour plots of the damage variable  $d$  for a double-edge-notched specimen with  $a = 28$  mm. To aid visualization, elements with an average value of  $d > 0.95$  have been removed from the plots.

**Table 2**  
Material properties for the double-edge-notched specimens of Hocine et al. (2002).

$G_0 = Nk_B\vartheta$	$n$	$\bar{E}_b = NnE_b$	$K$	$\varepsilon_R^f = Nn\varepsilon_b^f$	$\ell$	$\zeta$
0.268 MPa	1000	15 MPa	2.68 MPa	0.235 MJ/m <sup>3</sup>	1 mm	10 kPa·s

bottom edge of the specimen is fixed, while the top-edge is prescribed a displacement at a nominal stretch rate of  $1 \times 10^{-3}/s$ . The simulations are performed in plane-stress. The material parameters used in this set of simulations for the SBR elastomer of Hocine et al. (2002) are shown in Table 2. A large value of  $n = 1000$  is chosen to represent the essentially neo-Hookean response of the SBR elastomer. Also, the rather large value of  $\ell = 1$  mm is chosen for the pragmatic reasons discussed in the Remark on page 4.<sup>12</sup>

Fig. 9(b) shows the calculated force-displacement curves as solid lines for notches with initial lengths of

$a = 12, 16, 20, 24$ , and  $28$  mm.

<sup>12</sup> For large values of  $n$ , it is useful for numerical reasons to rewrite the implicit Eq. (4.4) for the bond-stretch as,

$$(1-d)^2 \bar{E}_b (\lambda_b - 1) - G_0 \left( \frac{\sqrt{n} \tilde{\lambda}}{\tilde{\lambda}_b^2} \right) \mathcal{L}^{-1} \left( \frac{\tilde{\lambda} \lambda_b^{-1}}{\sqrt{n}} \right) = 0. \quad (6.1)$$

As expected, as the initial length of a notch increases, the overall force level becomes lower, and the displacement at which final fracture occurs, becomes smaller. This figure also shows a comparison of load-deflection curves from the simulations against the experimental results of Hocine et al. (2002) (dashed-lines); there is an acceptable match between the simulations and the experimentally-measured results.

Fig. 10 shows the deformed geometry at points (a) through (h) on the force-displacement curve in Fig. 9(b) for  $a = 28\text{mm}$ , together with contours of the damage variable  $d$ , which are barely visible. To aid visualization of the damage, elements with an average value of  $d > 0.95$  are not plotted. Fig. 10(a) is the initial configuration. As the sample is stretched to (b) the notch is blunted, but no damage has initiated. Damage initiates when the sample is stretched further to a displacement level of  $\sim 60\text{mm}$  (a point just before (c)), but the force is still increasing, and it is after another  $\sim 3\text{ mm}$  of extension that the force reaches a peak at point (c) in force-displacement curve, and from the contour of damage shown in Fig. 10(c), a small damage zone ahead of the notch becomes observable. Further stretching begins the rupture process, and Figs. 10(d) through (h) show this progressive rupturing, with (h) showing the final failed configuration.

## 7. Conclusions

We have formulated a theory and developed a numerical simulation capability for progressive damage and rupture in elastomeric materials which accounts for the underlying microscopic behavior of molecular bond stretching and scission. Adopting this microscopic view should be useful for modeling elastomeric materials at small length scales, such as occurs in nano-composites and bio-inspired composites. When the flaw size is comparable in length to the material length scale  $\ell$ , the flaw sensitivity diverges from the predictions of classical energy release rate-based fracture mechanics, with the material showing much lower sensitivity to flaws than predicted by classical fracture mechanics. The proposed theory and its numerical implementation represents a step towards modeling this behavior, and perhaps optimizing the response of such materials at the small scale.

We have also shown that with a suitable choice of material parameters in our gradient-damage theory, that our numerical simulation capability may be used to reproduce the experimentally-measured force-deflection curves for fracture of double-edge-notched specimens which are tens of millimeters in size with millimeter-dimensioned cracks, in a styrene-butadiene (SBR) synthetic elastomer (Hocine et al., 2002).

The present work has focused on the simplest case of elastomeric materials which can undergo large reversible deformations with negligible rate-dependent dissipation. It would be useful to extend the ideas in our theory to materials which exhibit additional dissipation mechanism (e.g., viscoelasticity and Mullins effect) that accompany the rupture process, which can be exploited as toughening mechanisms (Ducrot et al., 2014; Mao et al., 2017a; Zhao, 2014).

## Acknowledgment

Support from Exxon-Mobil Research through the MIT Energy Initiative is gratefully acknowledged.

## Appendix A. Detailed derivation of the theory

In this Appendix we give details of our gradient-damage theory for fracture of a finitely-deforming elastic solid.

### A1. Kinematics

Consider a macroscopically homogeneous body  $B$  with the region of space it occupies in a fixed reference configuration, and denote by  $\mathbf{X}$  an arbitrary material point of  $B$ . A motion of  $B$  is then a smooth one-to-one mapping

$$\mathbf{x} = \chi(\mathbf{X}, t), \quad (\text{A.1})$$

with deformation gradient, velocity, and acceleration given by

$$\mathbf{F} = \nabla \chi, \quad \mathbf{v} = \dot{\chi}, \quad \dot{\mathbf{v}} = \ddot{\chi}. \quad (\text{A.2})$$

As is standard, we assume that

$$J \stackrel{\text{def}}{=} \det \mathbf{F} > 0. \quad (\text{A.3})$$

The right and left Cauchy-Green tensors are given respectively by

$$\mathbf{C} = \mathbf{F}^T \mathbf{F}, \quad \mathbf{B} = \mathbf{F} \mathbf{F}^T. \quad (\text{A.4})$$

We denote the distortional (or volume preserving) part of  $\mathbf{F}$  by

$$\bar{\mathbf{F}} \stackrel{\text{def}}{=} J^{-1/3} \mathbf{F}, \quad \det \bar{\mathbf{F}} = 1, \quad (\text{A.5})$$

and correspondingly let

$$\bar{\mathbf{C}} \stackrel{\text{def}}{=} \bar{\mathbf{F}}^T \bar{\mathbf{F}} = J^{-2/3} \mathbf{C}, \quad \bar{\mathbf{B}} \stackrel{\text{def}}{=} \bar{\mathbf{F}} \bar{\mathbf{F}}^T = J^{-2/3} \mathbf{B} \quad (\text{A.6})$$

denote the distortional right and left Cauchy-Green tensors.

We denote an arbitrary part of  $P$  by  $P$ , and by  $\mathbf{n}_R$  the outward unit normal on the boundary  $\partial P$  of  $P$ . Further, henceforth we use a subscript “ $R$ ” to refer to quantities measured in the reference configuration.

## A2. Effective bond stretch

Following [Mao et al. \(2017b\)](#) we introduce a dimensionless positive-valued internal variable,

$$\lambda_b > 0,$$

to represent (at the continuum scale) a measure of the stretch of the Kuhn segments of the polymer chains. We call  $\lambda_b$  the *effective bond stretch*.

## A3. Damage variable. Phase-field

To describe fracture we introduce an *damage variable* or *phase-field*,

$$d(\mathbf{X}, t) \in [0, 1]. \quad (\text{A.7})$$

If  $d = 0$  at a point then that point is intact, while if  $d = 1$  at some point, then that point is fractured. Values of  $d$  between zero and one correspond to partially-fractured material. We assume that  $d$  grows monotonically so that

$$\dot{d}(\mathbf{X}, t) \geq 0, \quad (\text{A.8})$$

which is a constraint that represents the usual assumption that microstructural changes leading to fracture are *irreversible*.

## A4. Principle of virtual power. Macroscopic and microscopic force balances

We follow [Gurtin \(1996, 2002\)](#) and [Gurtin et al. \(2010\)](#) to derive macroscopic and microscopic force balances derived via the principle of virtual power. In developing our theory we take the “rate-like” kinematical descriptors to be  $\dot{\chi}$ ,  $\dot{\mathbf{F}}$ ,  $\dot{\lambda}_b$ , and  $\dot{d}$ , and also the gradient  $\nabla d$ . In exploiting the principle of virtual power we note that the rates  $\dot{\chi}$  and  $\dot{\mathbf{F}}$  are not independent – they are constrained by (cf. [\(A.2\)](#))

$$\nabla \dot{\chi} = \dot{\mathbf{F}}. \quad (\text{A.9})$$

With each evolution of the body we associate macroscopic and microscopic force systems. The macroscopic system is defined by:

- (i) a traction  $\mathbf{t}_R(\mathbf{n}_R)$  (for each unit vector  $\mathbf{n}_R$ ) that expends power over the velocity  $\dot{\chi}$ ;
- (ii) a generalized external body  $\mathbf{b}_R$  that expends power over  $\dot{\chi}$ , where

$$\mathbf{b}_R = \mathbf{b}_{0R} - \rho_R \ddot{\chi}, \quad (\text{A.10})$$

- with  $\mathbf{b}_{0R}$  the non-inertial body force and  $\rho_R$  the mass density in the reference configuration; and
- (iii) a stress  $\mathbf{T}_R$  that expends power over the distortion rate  $\dot{\mathbf{F}}$ .

The microscopic system, which is non-standard, is defined by:

- (a) a scalar microscopic force  $f$  that expends power over the rate  $\dot{\lambda}_b$ ;
- (b) a scalar microscopic stress  $\varpi$  that expends power over the rate  $\dot{d}$ ;
- (c) a vector microscopic stress  $\xi$  that expends power over the gradient  $\nabla d$ ; and
- (d) a scalar microscopic traction  $\xi(\mathbf{n}_R)$  that expends power over  $d$ .

We characterize the force systems through the manner in which these forces expend power. That is, given any part  $P$ , through the specification of  $\mathcal{W}_{\text{ext}}(P)$ , the power expended on  $P$  by material external to  $P$ , and  $\mathcal{W}_{\text{int}}(P)$ , a concomitant expenditure of power within  $P$ . Specifically,

$$\left. \begin{aligned} \mathcal{W}_{\text{ext}}(P) &= \int_{\partial P} \mathbf{t}_R(\mathbf{n}_R) \cdot \dot{\chi} da_R + \int_P \mathbf{b}_R \cdot \dot{\chi} dv_R + \int_{\partial P} \xi(\mathbf{n}_R) \dot{d} da_R, \\ \mathcal{W}_{\text{int}}(P) &= \int_P \left( \mathbf{T}_R : \dot{\mathbf{F}} + f \dot{\lambda}_b + \varpi \dot{d} + \xi \cdot \nabla d \right) dv_R, \end{aligned} \right\} \quad (\text{A.11})$$

where,  $\mathbf{T}_R$ ,  $f$ ,  $\varpi$ , and  $\xi$ , are defined over the body for all time.

Assume that, at some arbitrarily chosen but *fixed time*, the fields  $\chi$ ,  $\mathbf{F}$ ,  $\lambda_b$ , and  $d$  are known, and consider the fields  $\dot{\chi}$ ,  $\dot{\mathbf{F}}$ ,  $\dot{\lambda}_b$ , and  $\dot{d}$  as virtual velocities to be specified independently in a manner consistent with [\(A.9\)](#); that is, denoting the virtual fields by  $\tilde{\chi}$ ,  $\tilde{\mathbf{F}}$ ,  $\tilde{\lambda}_b$ , and  $\tilde{d}$  to differentiate them from fields associated with the actual evolution of the body, we require that

$$\nabla \tilde{\chi} = \tilde{\mathbf{F}}. \quad (\text{A.12})$$

Further, we define a generalized virtual velocity to be a list

$$\mathcal{V} = (\tilde{\chi}, \tilde{\mathbf{F}}, \tilde{\lambda}_b, \tilde{d}),$$

consistent with (A.12).

We refer to a macroscopic virtual field  $\mathcal{V}$  as *rigid* if it satisfies

$$(\nabla \tilde{\chi}) = \tilde{\mathbf{F}} = \boldsymbol{\Omega} \mathbf{F} \quad \text{together with } \tilde{\lambda}_b = 0, \quad \tilde{d} = 0, \quad (\text{A.13})$$

with  $\boldsymbol{\Omega}$  a spatially constant skew tensor.

Next, writing

$$\left. \begin{aligned} \mathcal{W}_{\text{ext}}(P, \mathcal{V}) &= \int_{\partial P} \mathbf{t}_R(\mathbf{n}_R) \cdot \tilde{\chi} da_R + \int_P \mathbf{b}_R \cdot \tilde{\chi} dv_R + \int_{\partial P} \xi(\mathbf{n}_R) \tilde{d} da_R, \\ \mathcal{W}_{\text{int}}(P, \mathcal{V}) &= \int_P (\mathbf{T}_R : \tilde{\mathbf{F}} + f \tilde{\lambda}_b + \varpi \tilde{d} + \boldsymbol{\xi} \cdot \nabla \tilde{d}) dv_R, \end{aligned} \right\} \quad (\text{A.14})$$

respectively, for the external and internal expenditures of virtual power, the *principle of virtual power* consists of two basic requirements:

(V1) Given any part  $P$ ,

$$\mathcal{W}_{\text{ext}}(P, \mathcal{V}) = \mathcal{W}_{\text{int}}(P, \mathcal{V}) \quad \text{for all generalized virtual velocities } \mathcal{V}. \quad (\text{A.15})$$

(V2) Given any part  $P$  and a *rigid* virtual velocity  $\mathcal{V}$ ,

$$\mathcal{W}_{\text{int}}(P, \mathcal{V}) = 0 \quad \text{whenever } \mathcal{V} \text{ is a rigid macroscopic virtual velocity.} \quad (\text{A.16})$$

To deduce the consequences of the principle of virtual power, assume that (A.15) and (A.16) are satisfied. Note that in applying the virtual balance we are at liberty to choose any  $\mathcal{V}$  consistent with the constraint (A.12).

#### A5. Macroscopic force and moment balances

Let  $\tilde{\lambda}_b = 0$  and  $\tilde{d} = 0$ . For this choice of  $\mathcal{V}$ , (A.15) yields

$$\int_{\partial P} \mathbf{t}_R(\mathbf{n}_R) \cdot \tilde{\chi} da_R + \int_P \mathbf{b}_R \cdot \tilde{\chi} dv_R = \int_P \mathbf{T}_R : \tilde{\mathbf{F}} dv_R = \int_P \mathbf{T}_R : \nabla \tilde{\chi} dv_R, \quad (\text{A.17})$$

which may be rewritten as

$$\int_{\partial P} \mathbf{t}_R(\mathbf{n}_R) \cdot \tilde{\chi} da_R = \int_P (\mathbf{T}_R : \nabla \tilde{\chi} - \mathbf{b}_R \cdot \tilde{\chi}) dv_R, \quad (\text{A.18})$$

and using the divergence theorem we may conclude that

$$\int_{\partial P} (\mathbf{T}_R(\mathbf{n}_R) - \mathbf{T}_R \mathbf{n}_R) \cdot \tilde{\chi} da_R + \int_P (\text{Div } \mathbf{T}_R + \mathbf{b}_R) \cdot \tilde{\chi} dv_R = 0.$$

Since this relation must hold for all  $P$  and all  $\tilde{\chi}$ , standard variational arguments yield the traction condition

$$\mathbf{t}_R(\mathbf{n}_R) = \mathbf{T}_R \mathbf{n}_R, \quad (\text{A.19})$$

and the local macroscopic force balance

$$\text{Div } \mathbf{T}_R + \mathbf{b}_R = \mathbf{0}, \quad (\text{A.20})$$

respectively.

Next, we deduce the consequences of requirement (V2) of the principle of virtual power. Using (A.13) and (A.14)<sub>2</sub>, requirement (V2) of the principle of virtual power leads to the requirement that

$$\int_P (\mathbf{T}_R \mathbf{F}^T) : \boldsymbol{\Omega} dv_R = 0. \quad (\text{A.21})$$

Since  $P$  is arbitrary, we obtain that  $(\mathbf{T}_R \mathbf{F}^T) : \boldsymbol{\Omega} = 0$  for all skew tensors  $\boldsymbol{\Omega}$ , which implies that  $\mathbf{T}_R \mathbf{F}^T$  is symmetric:

$$\boxed{\mathbf{T}_R \mathbf{F}^T = \mathbf{F} \mathbf{T}_R^T.} \quad (\text{A.22})$$

- In view of (A.20) and (A.22) the stress  $\mathbf{T}_R$  represents the classical Piola stress, with (A.20) and (A.22) representing the local macroscopic force and moment balances in the reference body.

Upon using the expression (A.10) for  $\mathbf{b}_R$  in (A.20), we obtain the equation of motion

$$\boxed{\text{Div } \mathbf{T}_R + \mathbf{b}_{0R} = \rho_R \ddot{\chi}.} \quad (\text{A.23})$$

#### A6. Microscopic force balances

1. Next, consider a generalized virtual velocity with  $\tilde{\chi} = \mathbf{0}$  and  $\tilde{d} = 0$  and choose the virtual field  $\tilde{\lambda}_b$  arbitrarily. The power balance (A.15) then yields the microscopic virtual-power relation

$$0 = \int_P f \tilde{\lambda}_b d\nu_R, \quad (\text{A.24})$$

to be satisfied for all  $\tilde{\lambda}_b$  and all P, and a standard argument yields the microscopic force balance

$$f = 0. \quad (\text{A.25})$$

The requirement that  $f = 0$  implies that a variation of  $\lambda_b$  expends no internal power, and at first blush it appears that the “microforce balance” (A.25) is devoid of physical content. However, it does have physical content, which is revealed later when we consider our thermodynamically consistent constitutive theory in Section A.8. As we shall see (A.25) will imply an internal constraint equation between  $\lambda_b$  and the right Cauchy-Green tensor  $\mathbf{C}$  and other constitutive variables of the form  $f(\mathbf{C}, \lambda_b, d, \nabla d) = 0$ , which will serve as an implicit equation for determining  $\lambda_b$  in terms of the right Cauchy-Green tensor  $\mathbf{C}$  and the other constitutive variables; cf. Section A.9.

2. Next, consider a generalized virtual velocity with  $\tilde{\chi} = \mathbf{0}$  and  $\tilde{\lambda}_b = 0$ , and choose the virtual field  $\tilde{d}$  arbitrarily. The power balance (A.15) then yields the microscopic virtual-power relation

$$\int_{\partial P} \xi(\mathbf{n}_R) \tilde{d} da_R = \int_P (\varpi \tilde{d} + \boldsymbol{\xi} \cdot \nabla \tilde{d}) d\nu_R, \quad (\text{A.26})$$

to be satisfied for all  $\tilde{d}$  and all P. Equivalently, using the divergence theorem,

$$\int_{\partial P} (\xi(\mathbf{n}_R) - \boldsymbol{\xi} \cdot \mathbf{n}_R) \tilde{d} da_R + \int_P (\operatorname{Div} \boldsymbol{\xi} - \varpi) \tilde{d} d\nu_R = 0,$$

and a standard argument yields the microscopic traction condition

$$\xi(\mathbf{n}_R) = \boldsymbol{\xi} \cdot \mathbf{n}_R, \quad (\text{A.27})$$

and the microscopic force balance

$$\operatorname{Div} \boldsymbol{\xi} - \varpi = 0. \quad (\text{A.28})$$

Finally, using the traction conditions (A.19) and (A.26), the actual external expenditure of power is

$$\mathcal{W}_{\text{ext}}(P) = \int_{\partial P} (\mathbf{T}_R \mathbf{n}_R) \cdot \dot{\chi} da_R + \int_P \mathbf{b}_R \cdot \dot{\chi} d\nu_R + \int_{\partial P} (\boldsymbol{\xi} \cdot \mathbf{n}_R) \dot{d} da_R. \quad (\text{A.29})$$

As is standard, the Piola stress  $\mathbf{T}_R$  is related to the symmetric Cauchy stress  $\mathbf{T}$  in the deformed body by

$$\mathbf{T}_R = J \mathbf{T} \mathbf{F}^{-\top}, \quad (\text{A.30})$$

so that

$$\mathbf{T} = J^{-1} \mathbf{T}_R \mathbf{F}^{\top}. \quad (\text{A.31})$$

Further, it is convenient to introduce a new stress measure called the second Piola stress

$$\mathbf{T}_{RR} \stackrel{\text{def}}{=} \mathbf{F}^{-1} \mathbf{T}_R = J \mathbf{F}^{-1} \mathbf{T} \mathbf{F}^{-\top}, \quad (\text{A.32})$$

which is symmetric.

Next, differentiating (A.4)<sub>1</sub> results in the following expression for the rate of change of  $\mathbf{C}$ ,

$$\dot{\mathbf{C}} = \mathbf{F}^{\top} \dot{\mathbf{F}} + \dot{\mathbf{F}}^{\top} \mathbf{F}.$$

Hence, since  $\mathbf{T}_{RR}$  is symmetric,

$$\mathbf{T}_{RR} : \dot{\mathbf{C}} = 2 \mathbf{T}_{RR} : \mathbf{F}^{\top} \dot{\mathbf{F}} = 2 (\mathbf{F} \mathbf{T}_{RR}) : \dot{\mathbf{F}},$$

and upon using (A.32), the stress power  $\mathbf{T}_R : \dot{\mathbf{F}}$  may be alternatively written as

$$\mathbf{T}_R : \dot{\mathbf{F}} = \frac{1}{2} \mathbf{T}_{RR} : \dot{\mathbf{C}}. \quad (\text{A.33})$$

Thus the corresponding actual internal expenditure of power (A.12) may be written as

$$\mathcal{W}_{\text{int}}(P) = \int_P \left( \frac{1}{2} \mathbf{T}_{RR} : \dot{\mathbf{C}} + f \dot{\lambda}_b + \varpi \dot{d} + \boldsymbol{\xi} \cdot \nabla \dot{d} \right) d\nu_R. \quad (\text{A.34})$$

### A7. Free-energy imbalance

We develop the theory within a framework that accounts for the first two laws of thermodynamics. For isothermal processes the first two laws collapse into a single dissipation inequality which asserts that temporal changes in free energy of a part P be not greater than the power expended on P (cf, e.g., [Gurtin et al., 2010](#)). Thus, let  $\psi_R(\mathbf{X}, t)$  denote the free energy density per unit reference volume. Then, the *free-energy imbalance under isothermal conditions* requires that for each part P of B,

$$\overline{\int_P \psi_R dv_R} \leq \mathcal{W}_{\text{ext}}(P). \quad (\text{A.35})$$

Bringing the time derivative in (A.35) inside the integral, using  $\mathcal{W}_{\text{ext}}(P) = \mathcal{W}_{\text{int}}(P)$ , [Eq. \(A.34\)](#), and rearranging gives

$$\int_P \left( \dot{\psi}_R - \frac{1}{2} \mathbf{T}_{RR} : \dot{\mathbf{C}} - f \dot{\lambda}_b - \varpi \dot{d} - \boldsymbol{\xi} \cdot \nabla \dot{d} \right) dv_R \leq 0. \quad (\text{A.36})$$

Thus, since P was arbitrarily chosen, we obtain the following local form of the free-energy imbalance,

$$\dot{\psi}_R - \frac{1}{2} \mathbf{T}_{RR} : \dot{\mathbf{C}} - f \dot{\lambda}_b - \varpi \dot{d} - \boldsymbol{\xi} \cdot \nabla \dot{d} \leq 0. \quad (\text{A.37})$$

For later use we define the dissipation density  $\mathcal{D} \geq 0$  per unit reference volume per unit time by

$$\mathcal{D} = \frac{1}{2} \mathbf{T}_{RR} : \dot{\mathbf{C}} + f \dot{\lambda}_b + \varpi \dot{d} + \boldsymbol{\xi} \cdot \nabla \dot{d} - \dot{\psi}_R \geq 0. \quad (\text{A.38})$$

**Remark.** For brevity we have not discussed the transformation properties under a change in frame of the various fields appearing in our theory. Here, we simply note that all quantities in the free energy imbalance (A.37) are invariant under a change in frame ([Gurtin et al., 2010](#)).

### A8. Constitutive theory

Let  $\Lambda$  represent the list

$$\Lambda = \{\mathbf{C}, \lambda_b, d, \nabla d\}. \quad (\text{A.39})$$

Guided by (A.37), we begin by assuming constitutive equations for the free energy  $\psi_R$ , the stress  $\mathbf{T}_{RR}$ , the scalar microstresses  $f$  and  $\varpi$ , and the vector microstress  $\boldsymbol{\xi}$  are given by the constitutive equations

$$\psi_R = \hat{\psi}_R(\Lambda), \quad \mathbf{T}_{RR} = \hat{\mathbf{T}}_{RR}(\Lambda), \quad f = \hat{f}(\Lambda), \quad \varpi = \hat{\varpi}(\Lambda), \quad \boldsymbol{\xi} = \hat{\boldsymbol{\xi}}(\Lambda). \quad (\text{A.40})$$

Then,

$$\dot{\psi}_R = \frac{\partial \hat{\psi}_R(\Lambda)}{\partial \mathbf{C}} : \dot{\mathbf{C}} + \frac{\partial \hat{\psi}_R(\Lambda)}{\partial \lambda_b} \dot{\lambda}_b + \frac{\partial \hat{\psi}_R(\Lambda)}{\partial d} \dot{d} + \frac{\partial \hat{\psi}_R(\Lambda)}{\partial \nabla d} \cdot \nabla \dot{d}. \quad (\text{A.41})$$

Using (A.41) and substituting the constitutive [Eqs. \(A.40\)](#) into the free-energy imbalance (A.37), we find that it may then be written as

$$\left[ \frac{\partial \hat{\psi}_R(\Lambda)}{\partial \mathbf{C}} - \frac{1}{2} \hat{\mathbf{T}}_{RR}(\Lambda) \right] : \dot{\mathbf{C}} + \left[ \frac{\partial \hat{\psi}_R(\Lambda)}{\partial \lambda_b} - \hat{f}(\Lambda) \right] \dot{\lambda}_b + \left[ \frac{\partial \hat{\psi}_R(\Lambda)}{\partial d} - \varpi \right] \dot{d} + \left[ \frac{\partial \hat{\psi}_R(\Lambda)}{\partial \nabla d} - \boldsymbol{\xi} \right] \cdot \nabla \dot{d} \leq 0. \quad (\text{A.42})$$

We introduce an *energetic macrostress*  $(\mathbf{T}_{RR})_{\text{en}}$ , and *energetic microstresses*  $f_{\text{en}}$ ,  $\varpi_{\text{en}}$ , and  $\boldsymbol{\xi}_{\text{en}}$  through

$$(\mathbf{T}_{RR})_{\text{en}} \stackrel{\text{def}}{=} \frac{\partial \hat{\psi}_R(\Lambda)}{\partial \mathbf{C}}, \quad f_{\text{en}} \stackrel{\text{def}}{=} \frac{\partial \hat{\psi}_R(\Lambda)}{\partial \lambda_b}, \quad \varpi_{\text{en}} \stackrel{\text{def}}{=} \frac{\partial \hat{\psi}_R(\Lambda)}{\partial d}, \quad \boldsymbol{\xi}_{\text{en}} \stackrel{\text{def}}{=} \frac{\partial \hat{\psi}_R(\Lambda)}{\partial \nabla d}, \quad (\text{A.43})$$

and guided by (A.42) also introduce a *dissipative microstresses*  $f_{\text{diss}}$ ,  $\varpi_{\text{diss}}$ , and  $\boldsymbol{\xi}_{\text{diss}}$  through

$$(\mathbf{T}_{RR})_{\text{diss}} \stackrel{\text{def}}{=} \mathbf{T}_{RR} - (\mathbf{T}_{RR})_{\text{en}}, \quad f_{\text{diss}} \stackrel{\text{def}}{=} f - f_{\text{en}}, \quad \varpi_{\text{diss}} \stackrel{\text{def}}{=} \varpi - \varpi_{\text{en}}, \quad \boldsymbol{\xi}_{\text{diss}} \stackrel{\text{def}}{=} \boldsymbol{\xi} - \boldsymbol{\xi}_{\text{en}}. \quad (\text{A.44})$$

Using (A.43) and (A.44), leads to the following reduced dissipation inequality

$$(\mathbf{T}_{RR})_{\text{diss}} : \dot{\mathbf{C}} + f_{\text{diss}} \dot{\lambda}_b + \varpi_{\text{diss}} \dot{d} + \boldsymbol{\xi}_{\text{diss}} \cdot \nabla \dot{d} \geq 0. \quad (\text{A.45})$$

Next, as (special) constitutive equations for  $(\mathbf{T}_{RR})_{\text{diss}}$ ,  $f_{\text{diss}}$ ,  $\boldsymbol{\xi}_{\text{diss}}$ , and  $\varpi_{\text{diss}}$  we assume that tensor macrostress  $\mathbf{T}_{RR}$ , the scalar microstress  $f$  and the vector microstress  $\boldsymbol{\xi}$  are all *purely energetic* so that

$$(\mathbf{T}_{RR})_{\text{diss}} = \mathbf{0}, \quad f_{\text{diss}} = 0, \quad \boldsymbol{\xi}_{\text{diss}} = \mathbf{0}, \quad (\text{A.46})$$

while  $\varpi_{\text{diss}}$  is given by

$$\varpi_{\text{diss}} = \alpha + \zeta \dot{d}, \quad \text{with } \alpha = \hat{\alpha}(\Lambda) > 0, \quad \text{and } \zeta = \hat{\zeta}(\Lambda) > 0, \quad (\text{A.47})$$

so that the dissipation inequality (A.45) is satisfied, that is

$$\mathcal{D} = (\alpha + \zeta \dot{d}) \dot{d} > 0 \quad \text{whenever } \dot{d} > 0. \quad (\text{A.48})$$

From (A.43), (A.44), (A.46), and (A.47) the tensor macrostress  $\mathbf{T}_{\text{RR}}$ , the scalar microstress  $f$ ,  $\varpi$ , and the vector microstress  $\xi$  are given by the thermodynamically consistent constitutive equations

$$\mathbf{T}_{\text{RR}} = \underbrace{\frac{\partial \hat{\psi}_{\text{R}}(\Lambda)}{\partial \mathbf{C}}}_{\text{energetic}}, \quad f = \underbrace{\frac{\partial \hat{\psi}_{\text{R}}(\Lambda)}{\partial \lambda_b}}_{\text{energetic}}, \quad \varpi = \underbrace{\frac{\partial \hat{\psi}_{\text{R}}(\Lambda)}{\partial d}}_{\text{energetic}} + \underbrace{\hat{\alpha}(\Lambda) + \hat{\zeta}(\Lambda) \dot{d}}_{\text{dissipative}}, \quad \xi = \underbrace{\frac{\partial \hat{\psi}_{\text{R}}(\Lambda)}{\partial \nabla d}}_{\text{energetic}}. \quad (\text{A.49})$$

#### A9. Implicit equation for the bond stretch

The microforce balance (A.25), viz.

$$f = 0, \quad (\text{A.50})$$

together with the constitutive equation (A.49)<sub>2</sub> gives the thermodynamic constraint

$$\frac{\partial \hat{\psi}_{\text{R}}(\Lambda)}{\partial \lambda_b} = 0, \quad (\text{A.51})$$

which serves as an implicit equation for  $\lambda_b$ , in terms of the other constitutive variables ( $\mathbf{C}$ ,  $d$ ,  $\nabla d$ ).

#### A10. Evolution equation for the damage variable

The microforce balance (A.28), viz.

$$\text{Div} \xi - \varpi = 0, \quad (\text{A.52})$$

together with the constitutive equations (A.49) gives the evolution equation for the damage variable  $d$  as

$$\begin{aligned} \zeta \dot{d} &= F \quad \text{for } \dot{d} > 0, \quad \text{where} \\ F &\stackrel{\text{def}}{=} \left[ -\frac{\partial \hat{\psi}_{\text{R}}(\Lambda)}{\partial d} + \text{Div} \left( \frac{\partial \hat{\psi}_{\text{R}}(\Lambda)}{\partial \nabla d} \right) \right] - \hat{\alpha}(\Lambda). \end{aligned} \quad (\text{A.53})$$

Since  $\zeta$  is positive-valued,  $F$  must be positive for  $\dot{d}$  to be positive and the damage to increase.

**Remark.** To formulate a rate-independent theory, instead of (A.47), as a special constitutive equation for  $\varpi_{\text{diss}}$ , we assume that

$$\varpi_{\text{diss}} = \alpha \quad \text{with } \alpha = \hat{\alpha}(\Lambda) > 0, \quad (\text{A.54})$$

and in this case Eq. (A.53) reduces to the requirement that

$$F = 0 \quad \text{for } \dot{d} > 0; \quad (\text{A.55})$$

that is  $F = 0$  is a necessary condition for  $\dot{d} > 0$ . Thus, in the rate-independent limit we have

$$\dot{d} \geq 0, \quad F \leq 0, \quad \dot{d} F = 0, \quad (\text{A.56})$$

which are the Kuhn-Tucker conditions associated with damage evolution. It may be shown that in the rate-independent limit,  $\dot{d} > 0$  if and only if the *consistency condition*

$$\dot{F} = 0 \quad \text{when } F = 0 \quad (\text{A.57})$$

is satisfied. The consistency condition may be used to determine the value of  $d$  when it is non-zero.

The theory formulated in this Appendix is summarized in Section 2 in the main body of the paper.

## Appendix B. Some details of the numerical solution procedure

We have implemented our theory using a finite element method within the commercial finite element code Abaqus Dassault Systèmes (v. 6.14), through its user-defined element interface UEL.

First of all we need to calculate  $\lambda_b$  from the following implicit equation,

$$f = (1-d)^2 \frac{E_b}{k_B \vartheta} (\lambda_b - 1) \lambda_b - r \beta = 0, \quad (\text{B.1})$$

in which for simplicity, we have introduced th notation<sup>13</sup>

$$r \stackrel{\text{def}}{=} \frac{\bar{\lambda}}{\sqrt{n} \lambda_b}; \quad r_0 \stackrel{\text{def}}{=} \frac{1}{\sqrt{n} \lambda_b}. \quad (\text{B.2})$$

Thus given  $\mathbf{F}$  and  $d$  we can solve for  $r \in [0, 1]$  from (B.1) using Newton's procedure, with a Jacobian,

$$\frac{df}{dr} = -(1-d)^2 \frac{E_b}{k_B \vartheta} (2\lambda_b - 1) \lambda_b \frac{1}{r} - \left( \beta + r \frac{\partial \beta}{\partial r} \right). \quad (\text{B.3})$$

### B0.1. Residuals and Jacobians on displacements DOFs

The operator split method (Miehe et al., 2010a) is used to solve the linear momentum balance (2.8) and the microforce balance (2.10) in a staggered fashion. Neglecting body force and possible tractions, we have the residual for the displacements ( $\psi^A$  is the test function with the superscript indexing the associated node):

$$R_i^A = - \int_{B^e} \psi^A \operatorname{Div} \mathbf{T}_R d\nu_R = \int_{B^e} (T_R)_{im} \cdot \nabla_m \psi^A d\nu_R \equiv (\nabla_m \psi^A, (T_R)_{im}) \quad (\text{B.4})$$

The Jacobians are ( $\phi$  with the superscript is the test function here)

$$K_{ij}^{AB} = \left( \nabla_m \psi^A, \frac{\partial (T_R)_{im}}{\partial F_{j\beta}} \Big|_d \nabla_\beta \phi^B \right). \quad (\text{B.5})$$

By considering  $\mathbf{T}_R$  as a function of  $(\mathbf{F}, \lambda_b(\mathbf{F}, d), d)$  in our case, then by using the chain rule, we have

$$\frac{\partial (T_R)_{im}}{\partial F_{j\beta}} \Big|_d = \frac{\partial (T_R)_{im}}{\partial F_{j\beta}} \Big|_{\lambda_b, d} + \frac{\partial (T_R)_{im}}{\partial \lambda_b} \Big|_{\mathbf{F}, d} \frac{\partial \lambda_b}{\partial F_{j\beta}} \Big|_d \quad (\text{B.6})$$

$$\frac{\partial (T_R)_{im}}{\partial d} \Big|_{\mathbf{F}} = \frac{\partial (T_R)_{im}}{\partial d} \Big|_{\mathbf{F}, \lambda_b} + \frac{\partial (T_R)_{im}}{\partial \lambda_b} \Big|_{\mathbf{F}, d} \frac{\partial \lambda_b}{\partial d} \Big|_{\mathbf{F}} \quad (\text{B.7})$$

The three terms

$$\frac{\partial (T_R)_{im}}{\partial F_{j\beta}} \Big|_{\lambda_b, d}; \quad \frac{\partial (T_R)_{im}}{\partial \lambda_b} \Big|_{\mathbf{F}, d}; \quad \frac{\partial (T_R)_{im}}{\partial d} \Big|_{\mathbf{F}, \lambda_b} \quad (\text{B.8})$$

are all very easy to obtain.

In addition, we also need to know the following two terms.

$$\frac{\partial \lambda_b}{\partial F_{j\beta}} \Big|_d; \quad \frac{\partial \lambda_b}{\partial d} \Big|_{\mathbf{F}} \quad (\text{B.9})$$

In order to obtain these terms, we recall the equation to solve  $\lambda_b$ . Take derivatives on the first one we have  $A_{j\beta} dF_{j\beta} + Bd\lambda_b + Cdd = 0$ . Then

$$\frac{\partial \lambda_b}{\partial F_{j\beta}} \Big|_d = -B^{-1} A_{j\beta}; \quad \frac{\partial \lambda_b}{\partial d} \Big|_{\mathbf{F}} = -B^{-1} C \quad (\text{B.10})$$

### B0.2. Residuals and Jacobians on damage DOFs

$$R_d^A = (\psi^A, \zeta \dot{d}) + (\nabla \psi^A, \varepsilon_R^f \ell^2 \nabla d) + (\psi^A, \varepsilon_R^f d - 2(1-d)\mathcal{H}) \quad (\text{B.11})$$

Then

$$K_{dd}^{AB} = \left( \psi^A, \zeta \frac{\partial \dot{d}}{\partial d} \phi^B \right) + (\nabla \psi^A, \varepsilon_R^f \ell^2 \nabla \phi^B) + (\psi^A, (\varepsilon_R^f + 2\mathcal{H}) \phi^B) \quad (\text{B.12})$$

<sup>13</sup> Note that the parameters  $r$  and  $r_0$  defined here are not related to the rest length and deformed length of a single chain.

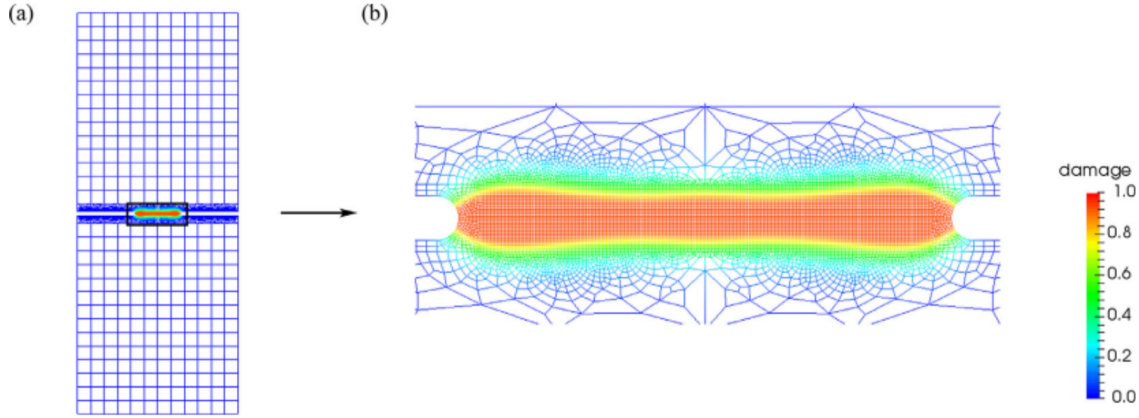


**Fig. 11.** Mesh for double edge notched thin sheets in tension. (a) Overall mesh (b) zoom in region for cracks.

and

$$K_{di}^{AB} = - \left( \psi^A, 2(1-d) \frac{\partial \mathcal{H}}{\partial F_{i\beta}} \nabla_\beta \phi^B \right) \quad (\text{B.13})$$

with  $\frac{\partial \mathcal{H}}{\partial F_{i\beta}}$  will evaluate numerically, and  $K_{d\mu}^{AB} = 0$ . As before,  $\frac{\partial d}{\partial t}$  depends on the time-integration scheme. In backward Euler,  $\frac{\partial d}{\partial t} = \frac{1}{\Delta t}$  with  $\Delta t$  is the time-step.

#### B0.3. Solution procedure setup

Quasi-static plane stress problems are considered. Linear approximants on triangular and quadrangular elements are used for both the phase-field  $d$  and the deformation map components  $\chi_i$ ,  $i = 1, 2$ . The phase-field is represented within Abaqus by treating it as the temperature field and specifying analysis steps of type \*COUPLED TEMPERATURE-DISPLACEMENT. Abaqus thus applies the backward Euler method for time integration of the microforce balance governing the phase-field evolution (2.10); see the Abaqus theory manual [Dassault Systèmes \(v. 6.14\)](#). Time integration accuracy is controlled with the option DELTMX, which specifies the maximum allowable nodal “temperature” change (actually the phase-field value in this case) between time increments. We have found that a limit of 0.02 provides a reasonable compromise between accuracy and computational efficiency.

The staggered solution procedure is invoked from the Abaqus input file by declaring \*SOLUTION TECHNIQUE, TYPE=SEPARATED in each load step. Default convergence criteria and tolerances are otherwise used.

#### B0.4. Weak plane stress algorithm

The plane stress condition is enforced using an algorithm similar to that described in [Klinkel and Govindjee \(2001\)](#). An implementation of the 3-dimensional version of the hyperelastic constitutive law of [Mao et al. \(2017b\)](#) is used. The condition

$$(T_R)_{33} = 0$$

is solved for the unknown out of plane stretch  $F_{33}$  with a Newton-Raphson iteration scheme, built on top of the constitutive law evaluation routine called during the assembly of the nodal residual forces and tangent stiffness matrices. After solution, static condensation of the material tangent stiffness operator is performed to get the plane stress tangent operator; see [Klinkel and Govindjee \(2001\)](#) for details.

For each call of the constitutive update at each quadrature point, we solve the implicit nonlinear Eq. (4.4) for  $\lambda_b$  with Newton-Raphson iteration supplemented with bisection using the `rtsafe` routine of [Press et al. \(1987\)](#). As noted in footnote 5 above, in computations, we modify the degradation function to

$$g(d) = (1-d)^2 + k,$$

where  $k$  is a small positive constant. This prevents complete loss of stress-bearing capacity of the material to avoid non-uniqueness of the solution. We have used a value of  $k \sim 10^{-4}$  in the simulations presented here.

#### Appendix C. An example of a mesh used in our simulations

For the simulations for double-edge-notched thin sheets in tension in [Section 6](#), a typical mesh that we used is displayed in [Fig. 11](#). The element size  $h_e$  is at the order of  $0.1\ell$ , with  $\ell$  the length-scale for the phase-field.

## References

- Anand, L., 1996. A constitutive model for compressible elastomeric solids. *Comput. Mech.* 18 (5), 339–355.
- Arruda, E.M., Boyce, M.C., 1993. A three-dimensional constitutive model for the large stretch behavior of rubber elastic materials. *J. Mech. Phys. Solids* 41 (2), 389–412.
- Azuma, C., Yasuda, K., Tanabe, Y., Taniguro, H., Kanaya, F., Nakayama, A., Chen, Y.M., Gong, J.P., Osada, Y., 2006. Biodegradation of high-toughness double network hydrogels as potential materials for artificial cartilage. *J. Biomed. Mater. Res. A*.
- Baer, E., Hiltner, A., Keith, H.D., 1987. Hierarchical structure in polymeric materials. *Science* 235 (4792), 1015–1022.
- Bourdin, B., Francfort, G.A., Marigo, J.-J., 2000. Numerical experiments in revisited brittle fracture. *J. Mech. Phys. Solids* 48 (4), 797–826.
- Buehler, M.J., 2006. Nature designs tough collagen: explaining the nanostructure of collagen fibrils. *Proc. Natl. Acad. Sci.* 103 (33), 12285–12290.
- Buehler, M.J., Abraham, F.F., Gao, H., 2003. Hyperelasticity governs dynamic fracture at a critical length scale. *Nature* 426 (6963), 141–146.
- Chen, C., Wang, Z., Suo, Z., 2016. Flaw sensitivity of highly stretchable materials. *Extreme Mech. Lett.* 10, 50–57.
- Cordier, P., Tournilhac, F., Soulié-Ziakovic, C., Leibler, L., 2008. Self-healing and thermoreversible rubber from supramolecular assembly. *Nat. Lett.* 451, 977–980.
- Dassault Systèmes, v. 6.14. Abaqus FEA. Computer software.
- Duarte, A., Coelho, J., Bordado, J., Cidade, M., Gil, M., 2012. Surgical adhesives: systematic review of the main types and development forecast. *Progress Polymer Sci.* 37 (8), 1031–1050.
- Ducrot, E., Chen, Y., Bulters, M., Sijbesma, R.P., Creton, C., 2014. Toughening elastomers with sacrificial bonds and watching them break. *Science* 344 (6180), 186–189.
- Gao, H., 2006. Application of fracture mechanics concepts to hierarchical biomechanics of bone and bone-like materials. *Int. J. Fract.* 138 (1–4), 101.
- Gao, H., Ji, B., Jäger, I.L., Arzt, E., Fratzl, P., 2003. Materials become insensitive to flaws at nanoscale: lessons from nature. *Proc. Natl. Acad. Sci.* 100 (10), 5597–5600.
- Griffith, A.A., 1921. The phenomena of rupture and flow in solids. *Philosophical transactions of the royal society of london. Series A, containing papers of a mathematical or physical character* 221, 163–198.
- Gurtin, M.E., 1996. Generalized Ginzburg-Landau and Cahn-Hilliard equations based on a microforce balance. *Physica D: Nonlinear Phenomena* 92 (3–4), 178–192.
- Gurtin, M.E., 2002. A gradient theory of single-crystal viscoplasticity that accounts for geometrically necessary dislocations. *Journal of the Mechanics and Physics of Solids* 50 (1), 5–32.
- Gurtin, M.E., Fried, E., Anand, L., 2010. The mechanics and thermodynamics of continua. Cambridge University Press.
- Hocine, N.A., Abdelaziz, M.N., Imad, A., 2002. Fracture problems of rubbers: J-integral estimation based upon  $\eta$  factors and an investigation on the strain energy density distribution as a local criterion. *International Journal of Fracture* 117 (1), 1–23.
- Holten-Andersen, N., Harrington, M.J., Birkedal, H., Lee, B.P., Messersmith, P.B., Lee, K.Y.C., Waite, J.H., 2010. pH-induced metal-ligand cross-links inspired by mussel yield self-healing polymer networks with near-covalent elastic moduli. *Proceedings of the National Academy of Sciences* 108 (7), 2651–2655.
- Jackson, A., Vincent, J., Turner, R., 1988. The mechanical design of nacre. *Proceedings of the Royal Society of London B: Biological Sciences* 234 (1277), 415–440.
- Kamat, S., Ballarini, R., Heuer, A.H., 2000. Structural basis for the fracture toughness of the shell of the conch strombus gigas. *Nature* 405, 1036–1040.
- Klinkel, S., Govindjee, S., 2001. Using finite strain 3d-material models in beam and shell elements. *Engineering Computations* 19 (3), 254–271.
- Kuhn, W., Grün, F., 1942. Beziehungen zwischen elastischen konstanten und dehnungs-doppelbrechung hochelastischer stoffe. *Kolloid-Zeitschrift* 101 (248).
- Lake, G.J., Thomas, A.G., 1967. The strength of highly elastic materials. *Proc. R. Soc. London, Ser. A* 300 (1460), 108–119.
- Lee, K.Y., Mooney, D.J., 2001. Hydrogels for tissue engineering. *Chem. Rev.* 101 (7), 1869–1879.
- Mao, Y., Lin, S., Zhao, X., Anand, L., 2017. A large deformation viscoelastic model for double-network hydrogels. *J. Mech. Phys. Solids* 100, 103–130.
- Mao, Y., Talamini, B., Anand, L., 2017. Rupture of polymers by chain scission. *Extreme Mech. Lett.* 13, 17–24.
- Miehe, C., Hofacker, M., Welschinger, F., 2010. A phase field model for rate-independent crack propagation: robust algorithmic implementation based on operator splits. *Comput. Methods Appl. Mech. Eng.* 199 (45), 2765–2778.
- Miehe, C., Schänzel, L.-M., 2014. Phase field modeling of fracture in rubbery polymers. Part I: finite elasticity coupled with brittle failure. *J. Mech. Phys. Solids* 65, 93–113.
- Miehe, C., Welschinger, F., Hofacker, M., 2010. Thermodynamically consistent phase-field models of fracture: Variational principles and multi-field fe implementations. *Int. J. Numer. Methods Eng.* 83 (10), 1273–1311.
- Nozoyama, T., Wada, S., Kiyama, R., Kitamura, N., Mredha, M.I., Zhang, X., Kurokawa, T., Nakajima, T., Takagi, Y., Yasuda, K., Gong, J.P., 2016. Double-network hydrogels strongly bondable to bones by spontaneous osteogenesis penetration. *Adv. Mater.* 28 (31), 6740–6745.
- Press, W.H., Flannery, B.P., Teukolsky, S.A., Vetterling, W.T., Kramer, P.B., 1987. Numerical recipes: the art of scientific computing. AIP.
- Raina, A., Miehe, C., 2016. A phase-field model for fracture in biological tissues. *Biomech. Modell. Mechanobiol.* 15 (3), 479–496.
- Rivlin, R.S., Thomas, A.G., 1952. Rupture of rubber. I. Characteristic energy for tearing. *J. Polymer Sci. X* (3), 291–318.
- Rottler, J., Barsky, S., Robbins, M.O., 2002. Cracks and crazes: on calculating the macroscopic fracture energy of glassy polymers from molecular simulations. *Phys. Rev. Lett.* 89 (14), 148304.
- Rottler, J., Robbins, M.O., 2003. Growth, microstructure, and failure of crazes in glassy polymers. *Phys. Rev. E* 68 (1), 011801.
- Schröder, J., Neff, P., 2003. Invariant formulation of hyperelastic transverse isotropy based on polyconvex free energy functions. *Int. J. Solids Struct.* 40, 401–445.
- Sen, D., Buehler, M.J., 2011. Structural hierarchies define toughness and defect-tolerance despite simple and mechanically inferior brittle building blocks. *Sci. Rep.* 1, 35.
- Sun, J., Bhushan, B., 2012. Hierarchical structure and mechanical properties of nacre: a review. *RSC Adv.* 2 (20), 7617–7632.
- Tokarev, I., Minko, S., 2009. Stimuli-responsive hydrogel thin films. *Soft Matter* 5, 511–524.
- Treloar, L.R.G., 1975. The physics of rubber elasticity. Oxford University Press, USA.
- Wu, J., McAuliffe, C., Waisman, H., Deodatis, G., 2016. Stochastic analysis of polymer composites rupture at large deformations modeled by a phase field method. *Comput. Methods Appl. Mech. Eng.* 312, 596–634.
- Zhao, X., 2014. Multi-scale multi-mechanism design of tough hydrogels: building dissipation into stretchy networks. *Soft Matter* 10 (5), 672–687.